PAPER

Multifunctional self-refrigerated multivariate {GdLn} (Ln = Dy, Tb, Tb/Eu) metal–organic frameworks†

Zhen Li, [ID] [ab] Ana Arauzo, [ID] [c] Claudio Roscini, [ID] [d] José Giner Planas [ID] *[a] and Elena Bartolomé [ID] *[a]

Multivariate metal–organic frameworks (MOFs) containing multiple lanthanide ions present a compelling avenue for developing versatile materials with tailored properties. In this work, we synthesized "self-refrigerated" multifunctional carborane-based MOFs of formula unit $\{[(GdLn)_3(mCB-L)_4(NO_3)(DMF)_x]_n \cdot Solv\}$ strategically combining Gd^{3+} ions, known for their ability to achieve large magnetocaloric effects (MCE), with various lanthanides (Ln = Dy, Tb, Eu, Tb/Eu) intended to act as Single Molecule Magnet (SMM) or/and luminescent units. The intricate magnetic, thermal, and optical properties of these multivariate Ln-MOFs were unraveled through a comprehensive characterization employing dc and ac magnetometry, X-ray Absorption Spectroscopy (XAS), X-ray Magnetic Circular Dichroism (XMCD), and luminescence measurements. Element-selective XAS-XMCD technique proved instrumental in elucidating the magnetic properties of the individual lanthanides, and their contribution to the macroscopic properties of the MOFs. We demonstrate that $Gd_{1.5}Ln_{1.5}$ (Ln = Tb, Dy) MOFs exhibit multifunctionality, incorporating MCE, field-induced magnetic relaxation dominated by the anisotropic ion, and green emission for Ln = Tb. Conversely, $Gd_{1.5}Ln_{1.5}$ (Ln = Eu, Eu/Tb) MOFs display MCE, field-induced SMM behavior associated with Gd, and red/yellow luminescent emission for Ln = Eu and Eu/Tb substitutions, respectively. Our findings significantly contribute to our understanding of "complex magnetic molecular materials" and set a pathway for the design of multifunctional multi-lanthanide MOFs endowed with tailored properties for various technological applications.

Introduction

Metal–organic frameworks (MOFs) have emerged as a versatile class of materials, showcasing unprecedented structural and compositional tunability that enables a wide range of applications in fields such as catalysis,[1] gas storage[2] and separation, drug delivery, magnetism,[3–5] *etc.* The deliberate incorporation of two or more metals into a single crystalline phase has given rise to multi-metallic multivariate (MTV) MOFs, unveiling additive or synergistic effects that sometimes surpass the individual contributions of their constituent elements.[6–8] These materials have been extensively explored for their unique properties, particularly in areas such as biomedical applications, catalysis, luminescent sensing, and more.[6,7] While multi-metallic MTV MOFs incorporating up to ten different transition metal ions have been well-studied for their specific characteristics,[8–13] a notable gap exists in our understanding of corresponding multi-lanthanide MOFs.[14] Remarkably, existing research primarily focuses on the luminescence properties of these mixed lanthanide-containing MOFs, with less attention paid so far to magnetic phenomena.[15–17]

Lanthanide MOFs (Ln MOFs) stand out as a distinct class of compounds featuring appealing optical, electronic, and magnetic properties resulting from 4f electrons. This makes them attractive for many applications, including luminescence,[18,19] anticounterfeiting,[20] sensors,[21–23] switching,[24] thermometry,[25] magnetic refrigeration,[26–29] conductive MOFs[30] and information storage and processing,[31,32] among others.

Indeed, the significant anisotropy of Ln(III) ions makes them excellent candidates for designing single-molecule magnets (SMMs), exhibiting magnetic stability and quantum-tunneling effects.[33–35] Recently, mononuclear SMMs with huge thermal activation energies close to 2000 K,[36] and open hysteresis loops above 80 K (ref. 37) have been demonstrated. Simultaneously,

[a] Institut de Ciència de Materials de Barcelona (ICMAB)-CSIC, Campus UAB, 08193-Bellaterra, Spain. E-mail: ebartolome@icmab.es; jginerplanas@icmab.es

[b] Shandong Provincial Key Laboratory of Monocrystalline Silicon Semiconductor Materials and Technology, College of Chemistry and Chemical Engineering, Dezhou University, Dezhou 253023, China

[c] Instituto de Nanociencia y Materiales de Aragón (INMA), CSIC-Universidad de Zaragoza, and Departamento de Física de la Materia Condensada, 50009 Zaragoza, Spain

[d] Catalan Institute of Nanoscience and Nanotechnology (ICN2) CSIC and Barcelona Institute of Science and Technology (BIST), Bellaterra, Barcelona 08193, Spain

† Electronic supplementary information (ESI) available. See DOI: https://doi.org/10.1039/d4ta03835e

This journal is © The Royal Society of Chemistry 2024

J. Mater. Chem. A, 2024, **12**, 21971–21986 | 21971

Ln(III) ions provide avenues for encoding molecular qubits for quantum computing.[38] The molecular platform offers the possibility to prepare reproducible qubits, at the limit of miniaturization, and push the scaling up, by encoding multiple qubits in one ion,[39,40] or by coupling the electronic spin with the nuclear spin.[41,42] The spatially ordered structures of MOFs present the potential to construct high-density information storage devices, incorporating SIMs as classical memory units in the nodes,[22,24,43–49] and also "quMOFs" of organized qubit arrays for quantum computing.[50,51]

On the other hand, Ln-MOFs are good candidates for ultra-low temperature cooling based on the magnetocaloric effect (MCE).[26–29] This effect exploits the entropy changes that result in the heating or cooling of the material when applying an external magnetic field at constant pressure. Magnetic refrigeration is an energy-efficient and environmentally friendly cooling technique that represents a significant advancement in sustainable cooling technology, particularly in the cryogenic regime, by eliminating the need for environmentally harmful refrigerants. In recent years, significant advancements have been made in magnetocaloric materials across various temperature ranges,[52] crucial for applications such as hydrogen liquefaction[53–55] and cryogenic refrigeration.[56,57] Recent reviews have highlighted the exceptional MCE performance of rare-earth based magnetocaloric materials,[58] including oxides,[59] intermetallics,[60] amorphous/high-entropy alloys, coordination polymers and MOFs.[28,29] Gd(III) ions, with $S = 7/2, L = 0, J = 7/2$, are ideal for obtaining a large MCE, since maximum entropy can be obtained from $S_{max} = Rln(2S + 1)$. Therefore, most MOFs reported for magnetic refrigeration are based on Gd, although proposals have been put forward to use anisotropic lanthanides to optimize the MCE performance of Ln-MOFs under lower magnetic field changes[61] and extend the operating temperature above 4 K.[62–64]

Interestingly, some Ln-MOFs can simultaneously incorporate several properties at the same time, such as magnetism along with luminescence,[17,65,66] or proton conductivity.[67,68] Moreover, the synthesis of multivariate mixed lanthanide MOFs can open new avenues for the development of multifunctional materials, combining different properties, or presenting new synergistic effects.

For instance, in lighting application, Ln(III) ions are known for their high color purity and significant quantum yields, particularly for those emitting red (Eu^{3+}) and green (Tb^{3+}) light.[20,66,69] Mixed Ln-MOFs have been frequently employed to tailor color emission by incorporating two or three Ln(III) ions in various proportions (commonly Eu/Tb,[20,70,71] but also other combinations such as La/Eu,[72] Gd/Eu,[70,72–74] Gd/Tb,[70,73,74] Gd/Sm,[74] Eu/Gd/Tb[75–77] or Ce/Eu/Tb[73]) and to achieve white-light emission.[73,77] This is often accomplished by combining Eu/Tb chromophores with blue-emitting ligands.[72,75–77] Moreover, mixed Ln-MOFs containing combinations like Eu/Tb,[78–81] Eu/Gd,[82] or Eu/Tb/Gd,[77] have been used to produce highly sensitive, ratiometric luminescent temperature sensors effective across a wide range of temperatures,[83] extending up to physiological levels.[80–82]

Meanwhile, in the field of magnetic refrigeration, mixed MOFs incorporating Gd and Tb with moderate ferromagnetic interactions have proven advantageous for improving MCE properties under low fields (<2 T), attainable by permanent magnets.[62] Furthermore, mixed Gd/Dy MOFs exhibited a shift of the maximum entropy change peak $-\Delta S_m$ towards higher temperatures with increasing the contents of Dy, while maintaining substantial $-\Delta S_m$ values, providing a route to expand the temperature range of magnetic cooling.[64]

Remarkably, in a recent work, we demonstrated the possibility of synthesizing multi-metallic multivariate (MTV) MOFs incorporating up to eight different rare-earth (RE) cations.[15] We emphasize that examples of multi-metallic MOFs with more than three 4f ions had never been reported before, due to compositional segregation issues during crystallization. This milestone was achieved thanks to the use of a 3D based carborane linker, mCB-L = 1,7-di(4-carboxyphenyl)-1,7-dicarba-$closo$-dodecaborane, which proved to be essential for the incorporation of different-sized RE cations.[15] Icosahedral carboranes represent a commercially accessible group of boron-rich clusters known for their remarkable stability.[84–86] They possess high hydrophobicity[85–91] and unconventional electronic structure, and are considered as inorganic 3D "aromatic" moieties.[92–94] Carborane-derived MOFs have been documented in literature,[95–105] and investigations, including our own, have demonstrated that integrating hydrophobic carborane linkers into MOF structures enhances their water stability.[106–109] This advancement has facilitated the development of aqueous inks for use in anti-counterfeiting and barcoding applications,[20] as well as MOF materials capable of trapping and degrading pesticides present in water.[110]

Significantly, our innovative carborane-based approach enables the creation of multi-metallic MOFs with any desired combination of lanthanide ions, facilitating the synthesis of multifunctional materials with tailored properties, and the investigation of novel "compositionally complex magnetic materials" with unexplored phenomena. In this work, we exploit this strategy to prepare "self-refrigerated" carborane-based MOFs of formula unit $\{[(GdLn)_3(m\text{CB-L})_4(NO_3)(DMF)_x]_n\cdot\text{Solv}\}$, where we combine Gd^{3+} ion, which is optimum to achieve large magnetocaloric effect (MCE), with various lanthanides (Ln = Dy, Tb, Eu, Tb/Eu) to provide added functionalities as SMM units or/and luminescent units. A comprehensive characterization, combining dc and ac magnetometry, X-ray Absorption Spectroscopy (XAS) and X-ray Magnetic Circular Dichroism (XMCD), along with luminescence measurements, will be used to provide insights into the intricate magnetic, thermal, and optical properties of these novel multivariate MOFs. Element-selective XAS-XMCD synchrotron technique will be crucially utilized to probe the magnetic properties of individual ions and elucidate how the overall magnetic and MCE properties depend on the constituent elements. We will discuss the multifunctional properties achieved for each GdLn MOF, depending on the lanthanide composition. Despite the increasing interest in multivariate MOFs,[7] applications of magnetic multi-lanthanide MOFs have been largely unexplored. Through this work, we aim to

21972 | J. Mater. Chem. A, 2024, 12, 21971–21986

This journal is © The Royal Society of Chemistry 2024

contribute to the holistic understanding of these complex magnetic materials, and lay the foundation for future advancements in the discovery of multifunctional multi-lanthanide MOFs, holding promise for various technological applications.

Experimental section

Synthesis

All chemicals were of reagent-grade quality. They were purchased from commercial sources and used as received. 1,7-di(4-carboxyphenyl)-1,7-dicarba-*closo*-dodecaborane ligand (mCBH$_2$L) was synthesized by a slight modification of a literature procedure.[111]

Synthesis of $\{[(Ln)_3(mCB-L)_4(NO_3)(DMF)_x]_n \cdot Solv\}$ (Ln = Gd/Eu, **Gd$_{1.5}$Eu$_{1.5}$**; Gd/Tb, **Gd$_{1.5}$Tb$_{1.5}$**; Gd/Dy, **Gd$_{1.5}$Dy$_{1.5}$**; Gd/Eu/Tb, **GdEuTb**). These compounds were synthesized following a previously described procedure.[15] In a typical preparation, mCB-L (0.03 mmol) and Ln(NO$_3$)$_3$ (0.02 mmol; Ln = Gd and Eu or Tb or Dy or Eu and Tb) were added to a mixture of DMF (0.5 mL)/methanol (1.5 mL)/H$_2$O (0.3 mL) and sonicated until complete dissolution of all reagents. The above mixture was transferred to an 8-dram vial and heated at 95 °C in an oven for 48 h. Needle like white crystals were collected and washed with DMF. Yield based on the Ln ions: 61% for **Gd$_{1.5}$Eu$_{1.5}$**, 63% for **Gd$_{1.5}$Tb$_{1.5}$**, 58% for **Gd$_{1.5}$Dy$_{1.5}$**, 62% for **GdEuTb**. IR (ATR; selected bands; cm^{-1}): 2601 (BH); 1658 (C=O from DMF); 1590 (C=O from carboxylate). $\{[(Gd_{0.48}Eu_{0.52})_3(mCB-L)_4(NO_3)(DMF)_x]_n \cdot Solv\}$ (**Gd$_{1.5}$Eu$_{1.5}$**). ICP(wt%): Gd(8.24 ± 0.1), Eu(8.76 ± 0.1). $\{[(Gd_{0.48}Tb_{0.52})_3(mCB-L)_4(NO_3)(DMF)_x]_n \cdot Solv\}$ (**Gd$_{1.5}$Tb$_{1.5}$**). ICP(wt%): Gd(9.4 ± 0.1), Tb(10.6 ± 0.1). $\{[(Gd_{0.47}Dy_{0.53})_3(mCB-L)_4(NO_3)(DMF)_x]_n \cdot Solv\}$ (**Gd$_{1.5}$Dy$_{1.5}$**). ICP(wt%): Gd(8.8 ± 0.1), Dy(10.36 ± 0.1). $\{[(GdEuTb)_3(mCB-L)_4(NO_3)(DMF)_x]_n \cdot Solv\}$ (**GdEuTb**). ICP(wt%): Gd(6.6 ± 0.1), Eu(7.0 ± 0.1), Tb(5.8 ± 0.1).

Instruments and characterization

Attenuated total reflection Fourier transformed infrared (ATR-FTIR) spectra were recorded using a PerkinElmer Spectrum One spectrometer equipped with a Universal ATR sampling accessory. Spectra were collected with 2 cm^{-1} spectral resolution in the 4000–650 cm^{-1} range. Elemental analyses were obtained by using a Thermo (Carlo Erba) Flash 2000 Elemental Analyser, configured for wt% CHN. Powder X-ray Diffraction (PXRD) was recorded at room temperature on a Siemens D-5000 diffractometer with Cu Kα radiation ($\lambda = 1.5418$ Å, 35 kV, 35 mA, increment = 0.02°). Inductively Coupled Plasma – Mass Spectrometry (ICP-MS) measurements were carried out in an Agilent ICP-MS 7700x apparatus. Scanning Electron Microscopy (SEM) (QUANTA FEI 200 FEGESEM) and optical microscopy (Olympus BX52) were used to monitor the morphology and color changes at various conditions. Solid state UV-visible spectra were obtained on a UV-vis-NIR V-780 spectrophotometer equipped with operational range of 200–1600 nm.

Dc magnetometry measurements in the temperature range 1.8 to 300 K were collected using a Quantum Design MPMS SQUID equipped with a 5 T magnet. Experiments were conducted on a powder samples embedded in Daphne oil to prevent grain orientation. Ac susceptibility measurements in the range between 1.8–9.0 K, at $\mu_0 H_{ac} = 4.1 \times 10^{-4}$ T, $\mu_0 H_{dc} = 0$–2.5 T in the range of frequencies between $f = 0.1$–1000 Hz were determined in the same SQUID magnetometer. Additional ac susceptibility measurements in the 10–10000 Hz range were carried out in a Quantum Design PPMS.

X-ray absorption spectroscopy (XAS) and X-ray magnetic circular dichroism (XMCD) experiments across the M$_{4,5}$ edges of Gd, Tb, Eu and Dy were performed at BOREAS beamline in ALBA synchrotron. The powdered samples were crashed on an indium foil and placed at the top of the cold finger. Measurements were performed at temperatures ranging between base temperature, 3.4 K ± 0.5 K, and 18 K. All spectra were recorded using Total Electron Yield (TEY) detection mode, with a 90% circularly polarized light. The XMCD ($\mu^- - \mu^+$) and XAS ($\mu^+ + \mu^-/2$) spectra at 6 T were determined from eight X-ray absorption spectra measured under right-handed (μ^+) and left-handed (μ^-) circular polarizations. XMCD(H) cycles were performed by following the resonant M$_5$ peak while sweeping the magnetic field between 6 T and −6 T at a rate of 2 T min^{-1}.

Luminescent emission spectra were obtained with PTI Quantamaster 300 fluorimeter, putting the solid powder in a custom-made holder and setting the holder plane at 45° with the direction of the incident light and the optical path towards the detector. All spectra were obtained irradiating with a continuous wave Xe lamp at $\lambda_{exc} = 280$ nm. Lifetime measurements were obtained with the same fluorimeter, but exciting at 280 nm with a pulsed Xe lamp (100 Hz, 2 μs integration time). Absolute luminescence quantum yields (Φ) of solid-state samples under continuous wave excitation ($\lambda_{exc} = 280$ nm) were determined using the Quantum Yield Fluorimeter Hamamatsu C9920-02G, equipped with an integrating sphere, connected to the lamp with an optical fiber, at room temperature in the air. Φ values were calculated based on the number of photons absorbed and emitted by the sample. A detailed measurement procedure can be found in a previous report.[112] Reported overall Φ values are averages of at least three independent determinations.

Results and discussion

Syntheses, structural and compositional characterization of the {GdLn} MOFs

$\{[(Gd_{0.48}Eu_{0.52})_3(mCB-L)_4(NO_3)(DMF)_x]_n \cdot Solv\}$ (**Gd$_{1.5}$Eu$_{1.5}$**), $\{[(Gd_{0.48}Tb_{0.52})_3(mCB-L)_4(NO_3)(DMF)_x]_n \cdot Solv\}$ (**Gd$_{1.5}$Tb$_{1.5}$**), $\{[(Gd_{0.47}Dy_{0.53})_3(mCB-L)_4(NO_3)(DMF)_x]_n \cdot Solv\}$ (**Gd$_{1.5}$Dy$_{1.5}$**) and $\{[(GdEuTb)_3(mCB-L)_4(NO_3)(DMF)_x]_n \cdot Solv\}$ (**GdEuTb**) were obtained as colorless crystals by solvothermal reactions in a mixture of DMF/methanol/H$_2$O at 95 °C for 48 h (see Experimental section for details). Powder X-ray diffraction (PXRD) data for all the synthesized {GdLn} MOFs (Fig. 1a) reveal these materials are isostructural with the mono- and multi-metal MOFs of the same family (see ESI Fig. S1†).[15,20] Thus, we only briefly describe here the main structural characteristics to facilitate the understanding of the magnetic properties of the newly reported mixed MOFs. Fig. 1b shows a view of the 3D
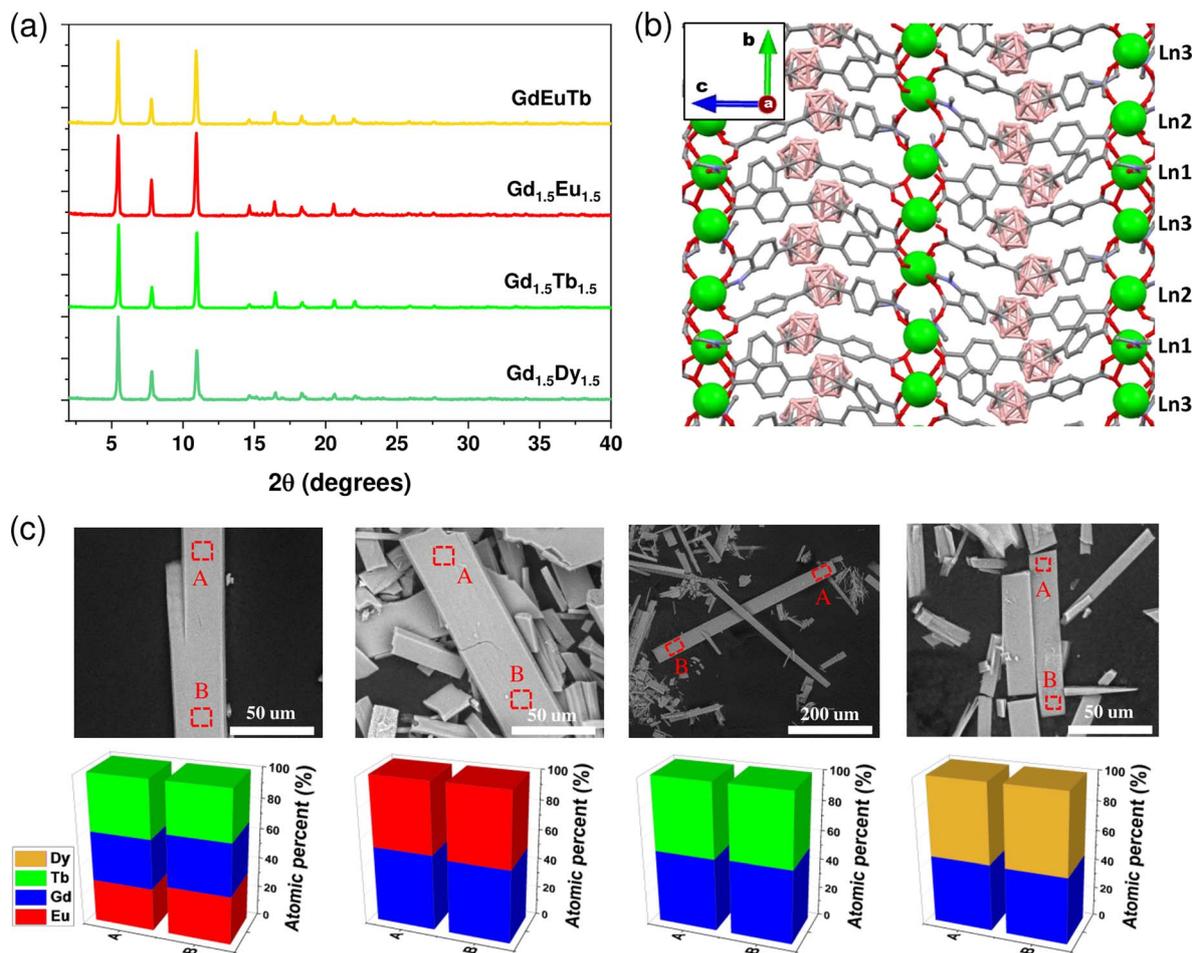
This journal is © The Royal Society of Chemistry 2024

J. Mater. Chem. A, 2024, **12**, 21971–21986 | **21973**

Fig. 1 Structural characterization of mixed {GdLn} MOFs. (a) Experimental Powder X-ray diffraction patterns for **GdEuTb** (yellow), **Gd$_{1.5}$Eu$_{1.5}$** (red), **Gd$_{1.5}$Tb$_{1.5}$** (green) and **Gd$_{1.5}$Dy$_{1.5}$** (dark green). (b) A view of the extended 3D framework for this MOF family along the *a*-axis, showing the Ln 1D-chains running along the *b*-axis, formed by three sites (Ln1, Ln2, Ln3) with non-equivalent coordination environments and the carborane linker *m*CB-L; Colour code: Ln (green), O (red), B (orange), C (grey); N (blue); H atoms and DMF molecules are omitted for clarity. (c) SEM images (from left to right) of **GdEuTb**, **Gd$_{1.5}$Eu$_{1.5}$**, **Gd$_{1.5}$Tb$_{1.5}$** and **Gd$_{1.5}$Dy$_{1.5}$** and EDX analysis of point scans of the Ln metals on the indicated positions (A and B) in the crystals.

structure for this family of MOFs, while a detailed description of the single crystal structure of previously published mono-metallic MOFs can be seen in Fig. S2.† The structure for these lanthanide family of carborane MOFs consists of 1D-chains of Ln cations along the *b* axis that are connected through the carborane dicarboxylic linkers to form the observed 3D structures (Fig. 1a and S2†). It is important to remark that the 1D-chains of Ln cations are formed by the repetition of three crystallographically non-equivalent Ln(III) ions (Ln1, Ln2, Ln3; indicated in Fig. 1b), each with different coordination environments. Three different Ln···Ln distances (Ln1···Ln2, 4.6–4.7 Å; Ln2···Ln3, 5.3 Å; Ln1···Ln3, 4.6 Å)[15,20] are found in the 1D-chains as a consequence of the non-equivalent positions of the three Ln ions. There can be found two distinct inter-chain distances in the 3D structure due to the arrangement of the carborane linkers (*ca.* 11 Å and 17 Å; Fig. S2†).

Analyses of the {GdLn} MOFs crystals by Scanning electron microscopy (SEM)/Energy dispersive X-ray (EDX) spectroscopy show a similar morphology to those previously reported (Fig. 1c).[15,20] In addition, EDX analysis at various points in the crystals confirm an equimolar distribution of Ln ions, ruling out compositional segregation and being consistent with multi-metallic MTV MOF composition.[14,15]

Magneto-thermal properties

The dc magnetic properties and MCE of all {GdLn} MOFs were characterized by SQUID magnetometry. For each MOF, we measured the temperature dependence of the susceptibility-temperature product at 0.1 T, $\chi T(T)$, and the field-dependence of the magnetization, $M(H)$, at different temperatures between 1.8 K and 12 K. From the later, the temperature dependence of the entropy change, $-\Delta S_m$, for different applied magnetic field changes $\Delta B = (B_f - 0)$ between $B_f = 0.5$–5 T was determined, following the Maxwell method.[113] Results are summarized in Fig. 2.

For **Gd$_{1.5}$Dy$_{1.5}$** MOF the χT product at 300 K reaches a value of 33.1 emu K mol^{-1}, close to the expected value for 1.5 Gd^{3+} and 1.5 Dy^{3+} ions per f.u., where the theoretical saturation for
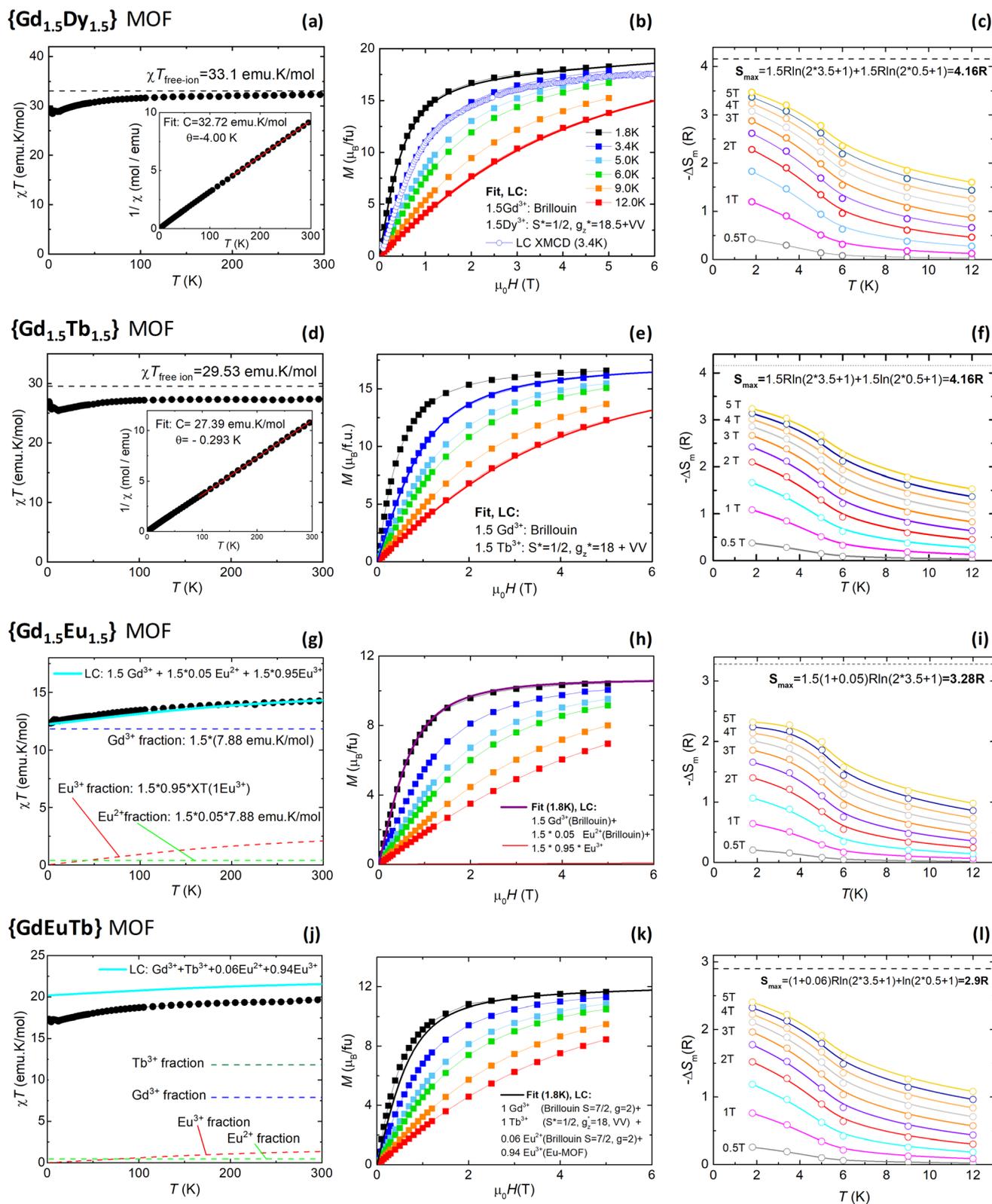
21974 | *J. Mater. Chem. A*, 2024, **12**, 21971–21986

This journal is © The Royal Society of Chemistry 2024

Fig. 2 Dc magnetometry and MCE properties for {GdLn} MOFs (**Gd$_{1.5}$Dy$_{1.5}$**, **Gd$_{1.5}$Tb$_{1.5}$**, **Gd$_{1.5}$Eu$_{1.5}$** and **GdEuTb**). (Left column: a, d, g and j): temperature dependence of the susceptibility product, χT, at 0.1 T; (central column: b, e, h and k): magnetization as a function of the applied magnetic field for different temperatures between 1.8–12 K; (right column: c, f, i and l): change of magnetic entropy as a function of the temperature for selected changes of applied magnetic field $\Delta B = B_f - 0$.

each ion, given by $\chi T_{\text{free ion}} = g_J^2 J(J + 1)/8$ (g_J the Landé constant and J the total angular momentum), is 7.9 emu K mol^{-1} (Gd^{3+}) and 14.1 emu K mol^{-1} (Dy^{3+}), see Fig. 2a. Upon decreasing the temperature, the χT product decreases down to 28.48 emu K mol^{-1} at 3.8 K, and then slightly increases for lower temperatures reaching a value of 29.45 emu K mol^{-1} at 1.8 K, evidencing the existence of weak intrachain ferromagnetic (FM) interactions. In the homonuclear Dy MOF analogue, such intrachain Ln–Ln interactions were also found to be FM,[114] estimated of the order $J_z^*/k_B \approx 0.45$ K, and practically negligible for isostructural Gd MOF.[115] On the other hand, the linear fit of the $1/\chi$ plot at high temperatures yields a Curie–Weiss temperature of $\theta = -4.00$ K, evidencing overall antiferromagnetic (AF) interactions, possibly of dipolar origin.

The $M(H)$ curves at all temperatures measured for **Gd$_{1.5}$Dy$_{1.5}$** MOF could be reasonably fit using a weighted linear combination of the magnetization predictions for Gd (using a Brillouin model with $S = 7/2$, $g = 2$), and the $M(H)$ curves for Dy within an Ising model, with effective spin $S^* = 1/2$, $g_z^* = 18.5$, $g_x^* = g_y^* = 0$, a van Vleck contribution $M_{VV} = H \cdot 0.19 \; \mu_B \; T^{-1}$ and negligible interactions ($J^* = 0$) (Fig. 2b).

The magnetic entropy change $-\Delta S_m(T, \Delta B)$ obtained for **Gd$_{1.5}$Dy$_{1.5}$** for selected field changes ΔB are shown in Fig. 2c. For practical purposes it is useful to discuss results obtained for $B_f = 2$ T, which is easily attained with permanent magnets in magnetic refrigerator applications. Thus, for $\Delta B = 2$–0 T the maximum value is found $-\Delta S_m^{max} = 2.28$ R (7.90 J kg^{-1} K^{-1}) at 1.8 K. This is a 55% of the magnetic entropy available for this mixed **Gd$_{1.5}$Dy$_{1.5}$** MOF: $S_{max} = 1.5$Rlog$(2 \cdot 3.5 + 1) + 1.5$Rlog$(2 \cdot 0.5 + 1) = 4.16$ R.

In the case of **Gd$_{1.5}$Tb$_{1.5}$** MOF, the χT product at 300 K saturates to 29.53 emu K mol^{-1}, approaching the expected value for the combination of 1.5 Gd^{3+} ions and 1.5 Tb^{3+} ions ($\chi T_{\text{free ion}}$ for Tb = 11.8 emu K mol^{-1}), see Fig. 2d. Similar to previous **Gd$_{1.5}$Dy$_{1.5}$** MOF, the $\chi T(T)$ product decreases upon cooling down to 25.42 emu K mol^{-1} at 12 K, and then slightly raises reaching 26.95 emu K mol^{-1} at 1.8 K, again pointing to the existence of weak intra-chain FM interactions. Homonuclear Tb MOF counterpart also presented weak FM intra-chain interactions.[114]

For **Gd$_{1.5}$Tb$_{1.5}$** MOF the $M(H)$ isotherms could be fit using a weighted linear combination of the Brillouin prediction for Gd, and the $M(H)$ curves for Tb, again within an Ising model, with effective spin $S^* = 1/2$, $g_z^* = 18$, $g_x^* = g_y^* = 0$, a smaller van Vleck contribution $M_{VV} = H \cdot 0.35 \; \mu_B \; T^{-1}$ and negligible interactions (Fig. 2e).

The magnetic entropy change $-\Delta S_m(T, \Delta B)$ obtained for **Gd$_{1.5}$Tb$_{1.5}$** from its magnetization isotherms, is shown in Fig. 2f. For $\Delta B = 2$ T it reaches a maximum value of $-\Delta S_m^{max} = 2.098$ R (7.28 J kg^{-1} K^{-1}) at 1.8 K, that is, a 50.4% of the maximum magnetic entropy available ($S_{max} = 4.16$ R).

In the case of **Gd$_{1.5}$Eu$_{1.5}$** MOF, the χT product does not saturate at high temperatures, owing to the Europium contribution. Moreover, the saturation of the $M(H, 1.8$ K) at 5 T is above the predicted value for 1.5 Gd^{3+} ions (10.5 μ_B), and given that Eu^{3+} is non-magnetic, it implies this MOF contains a small fraction of Eu^{2+} ($S = 7/2$) magnetic ions. Indeed, both the

saturation of the $\chi T(T)$ plot and the $M(H, 1.8$ K) curve could be well reproduced considering a 5% of Eu^{2+} of all Eu ions. The presence of Eu^{2+} in these synthesized MOFs arises from impurities in the precursor salts,[15] and the Eu^{2+}/Eu^{3+} ratio can be further increase upon X-ray irradiation (*vide infra* XMCD section).

The magnetic entropy change $-\Delta S_m(T, \Delta B)$ obtained for **Gd$_{1.5}$Eu$_{1.5}$**, see Fig. 2i, reaches $-\Delta S_m^{max} = 1.4$ R (4.84 J kg^{-1} K^{-1}) at 1.8 K for a $\Delta B = 2$ T, that is a 43% of the maximum magnetic entropy available (including the small Eu^{2+} contribution): $S_{max} \approx (1.5 + 0.05 \cdot 1.5)$Rlog$(2 \cdot 3.5 + 1) = 3.28$ R. For **GdEuTb** MOF, like in the **Gd$_{1.5}$Eu$_{1.5}$** instance discussed above, the $\chi T(T)$ and $M(H, 1.8$ K) curves reflect the presence of a small fraction of Eu^{2+} ions, see Fig. 2j and k, and both curves can be reasonably reproduced considering a linear combination of the theoretical curves for 1 Tb^{3+}, 0.94 Eu^{3+}, and 0.06 Eu^{2+} ions. For **GdEuTb** the determined magnetic entropy change $-\Delta S_m(T, \Delta B)$ reaches $-\Delta S_m^{max} = 1.52$ R (4.94 J kg^{-1} K^{-1}) at 1.8 K for a $\Delta B = 2$ T (Fig. 2l), that is a 52% of the maximum available magnetic entropy, $S_{max} \approx (1 + 0.06)$Rlog$(2 \cdot 3.5 + 1) + Rln(2 \cdot 0.5 + 1) = 2.9$ R.
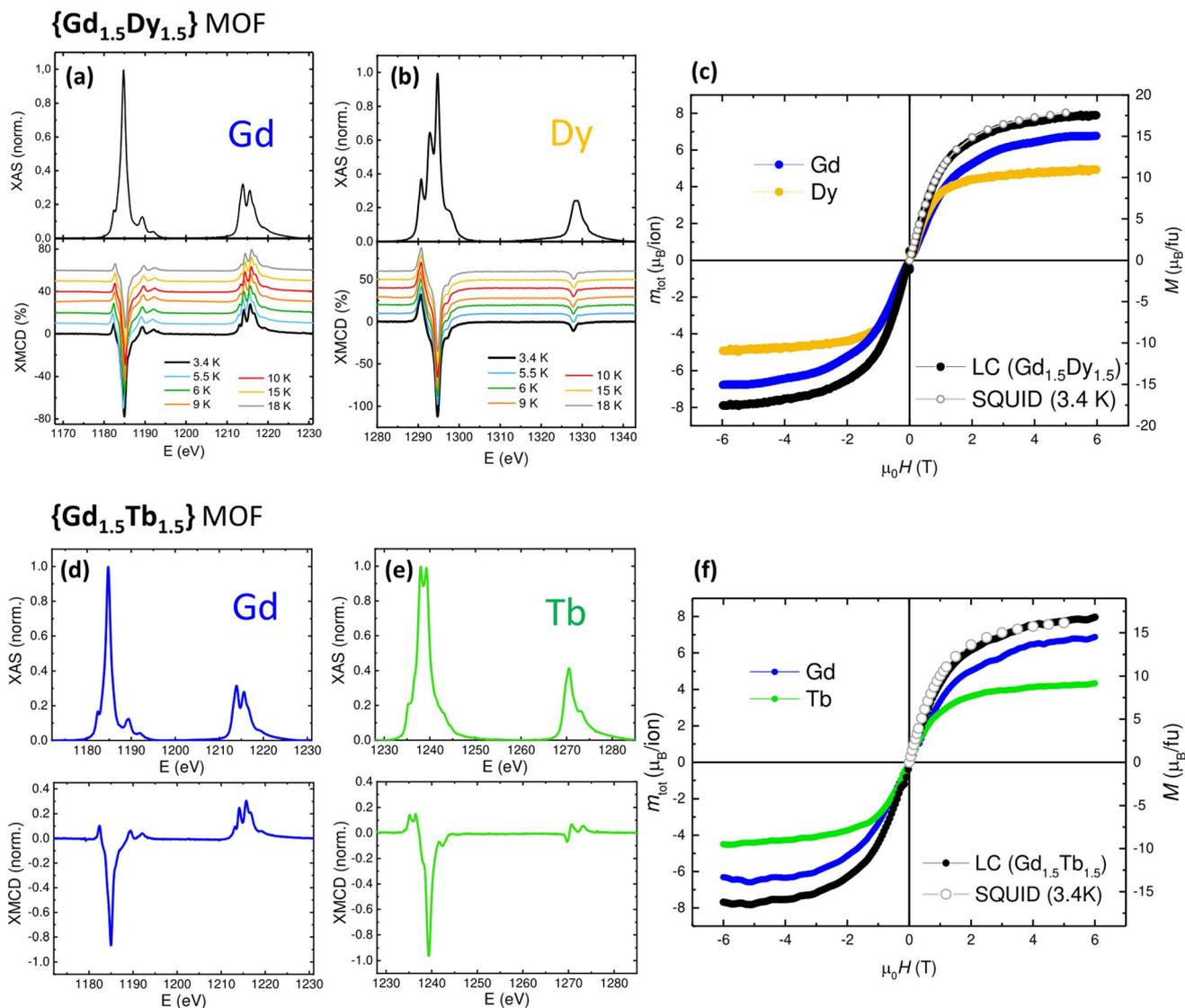
XAS and XMCD characterization

To investigate the magnetic properties and spectroscopic characteristics of the individual ions within the mixed {GdLn} MOF we used element-selective X-ray absorption spectroscopy (XAS) and X-ray magnetic circular dichroism (XMCD) technique. We performed XAS and XMCD measurements across the M$_{4,5}$ edges of Gd and Ln = Dy, Tb, Eu ions at 3.4 K and 6 T in each {GdLn} MOF. The orbital (m_L), spin (m_s) and total magnetic moment ($m_{TOT} = m_L + m_s$) for each ion were determined from the XAS-XMCD spectra using the corrected sum rules for lanthanides[116,117] (see Table S1†). The field-dependence of the total magnetic moment, $m_{tot}(H)$, for each Ln ion was determined by following the intensity of the XMCD(H) peak at the M$_5$ edge between -6 T and 6 T, and scaling the curve with the value of m_{TOT} obtained at 6 T.

Fig. 3 summarizes results for **Gd$_{1.5}$Dy$_{1.5}$** and **Gd$_{1.5}$Tb$_{1.5}$**, while Fig. 4 displays results for **Gd$_{1.5}$Eu$_{1.5}$** and **GdEuTb**. In all compounds, the Gadolinium XAS spectrum exhibits the expected features for trivalent Gd(III), see Fig. 3a, d, 4a and d: the M$_5$ edge shows a shoulder at 1182.4 eV, a main peak at 1184.7 and two satellites at 1189.3 and 1192.0 eV, whereas M$_4$ edge exhibits two peaks at 1213.92, 1215.6 eV and a shoulder at 1218.6 eV. The Gd XMCD spectrum across M$_5$ displays a main negative peak at 1184.85 eV and M$_4$ edge displays a positive pre-peak (1213.07 eV), two main peaks (1214.07, 1215.6 eV) a shoulder at 1216.52 eV and satellite at 1218.93 eV.

In **Gd$_{1.5}$Dy$_{1.5}$**, the XAS and XMCD spectra measured at Dysprosium M$_{4,5}$ edges are typical for Dy(III) (Fig. 3b). The XAS spectrum displays two pre-peaks (1296.71, 1292.88 eV), a main peak (1294.7 eV) at M$_5$ and a shoulder (1297.16 eV), while M$_4$ includes two close peaks (1328.1–1328.9 eV). The XMCD spectra consists of negative peaks, across M$_5$ a main peak at 1294.7 eV and a minor 1294.16 eV, and a small peak at M$_4$ (1327.8 eV). Fig. 3c shows the magnetic field dependence of the total magnetic moment per ion, $m_{TOT}(H)$, obtained at 3.4 K for Gd^{3+}

21976 | *J. Mater. Chem. A*, 2024, **12**, 21971–21986

This journal is © The Royal Society of Chemistry 2024

Fig. 3 XAS and XMCD characterization. **Gd$_{1.5}$Dy$_{1.5}$**: normalized, background-subtracted XAS (top) and XMCD (bottom) spectra measured across the M$_{4,5}$ edge of Gd (a) and Dy (b) at 6 T and indicated temperatures, between 3.4 K and 18 K; (c) field-dependence of the total magnetic moment, $m_{\text{TOT}}(H)$/ion, obtained for Gd^{3+} and Dy^{3+}, and magnetic moment per formula unit, at 3.4 K. Open symbols show, for comparison, the magnetization curve $M(H)$ of the mixed MOF determined by SQUID at the same temperature; **Gd$_{1.5}$Tb$_{1.5}$**: XAS and XMCD (6 T and 3.4 K) across the M$_{4,5}$ edges of Gd (d) and Tb (e); (f) $m_{\text{TOT}}(H)$/ion obtained for Gd^{3+} and Tb^{3+}, calculated magnetic moment per formula unit at 3.4 K (black filled symbols), and SQUID determined $M(H)$ (open symbols).

and Dy^{3+} in **Gd$_{1.5}$Dy$_{1.5}$**. They coincide with the $M(H)$ curves measured separately in the homonuclear Gd and Dy-MOFs.[114] Furthermore, we calculated the magnetic moment per formula unit, $m_{\text{Gd1.5Dy1.5}}$ (H), by taking a weighted linear combination (LC) of the $m_{\text{TOT}}(H)$ for each ion: $m_{\text{Gd1.5Dy1.5}} = 1.5 \cdot m_{\text{TOT}}(H)/$ion(Gd^{3+}) + $1.5 \cdot m_{\text{TOT}}(H)/$ion(Dy^{3+}). This calculated value is in excellent agreement with the magnetization curve, $M(H)$, measured by SQUID magnetometry for the mixed **Gd$_{1.5}$Dy$_{1.5}$** MOF, at the same temperature (3.4 K).

As for **Gd$_{1.5}$Tb$_{1.5}$**, the XAS and XMCD spectra at Terbium M$_{4,5}$ edges show the typical feature expected for Tb(III) (Fig. 3e). The XAS spectrum exhibits a pre-peak (1235.19 eV) and two main peaks (1237.99 eV) and shoulder (1242.99 eV) in the M$_5$ region, while M$_4$ consists of a peak at 1270.53 eV and shoulder (1273.2

eV). The XMCD spectra contain a primary negative peak at 1239.3 eV in the M$_5$ region and a minor peak at 1242.37 eV, and three features in the M$_4$ region (at 269.65, 1270.6, 1273.25 eV). Fig. 3f displays the $m_{\text{TOT}}(H)$/ion curves measured at 3.4 K for both Gd^{3+} and Tb^{3+} ions in **Gd$_{1.5}$Tb$_{1.5}$**. Similar to the above described compound, these curves align, respectively, with the $M(H)$ curves previously measured in the isostructural pure Gd and Tb MOFs.[114,115] Also, the magnetic moment per formula unit, calculated as the weighted LC of the ionic $m_{\text{TOT}}(H)$ contributions: $m_{\text{Gd1.5Tb1.5}}$ = $1.5 \cdot m_{\text{TOT}}(H)/$ion(Gd^{3+}) + $1.5 \cdot m_{\text{TOT}}(H)/$ion(Tb^{3+}), is in very good agreement with the magnetization SQUID-determined $M(H, 3.4 \text{ K})$ curve for **Gd$_{1.5}$Tb$_{1.5}$**.

This journal is © The Royal Society of Chemistry 2024

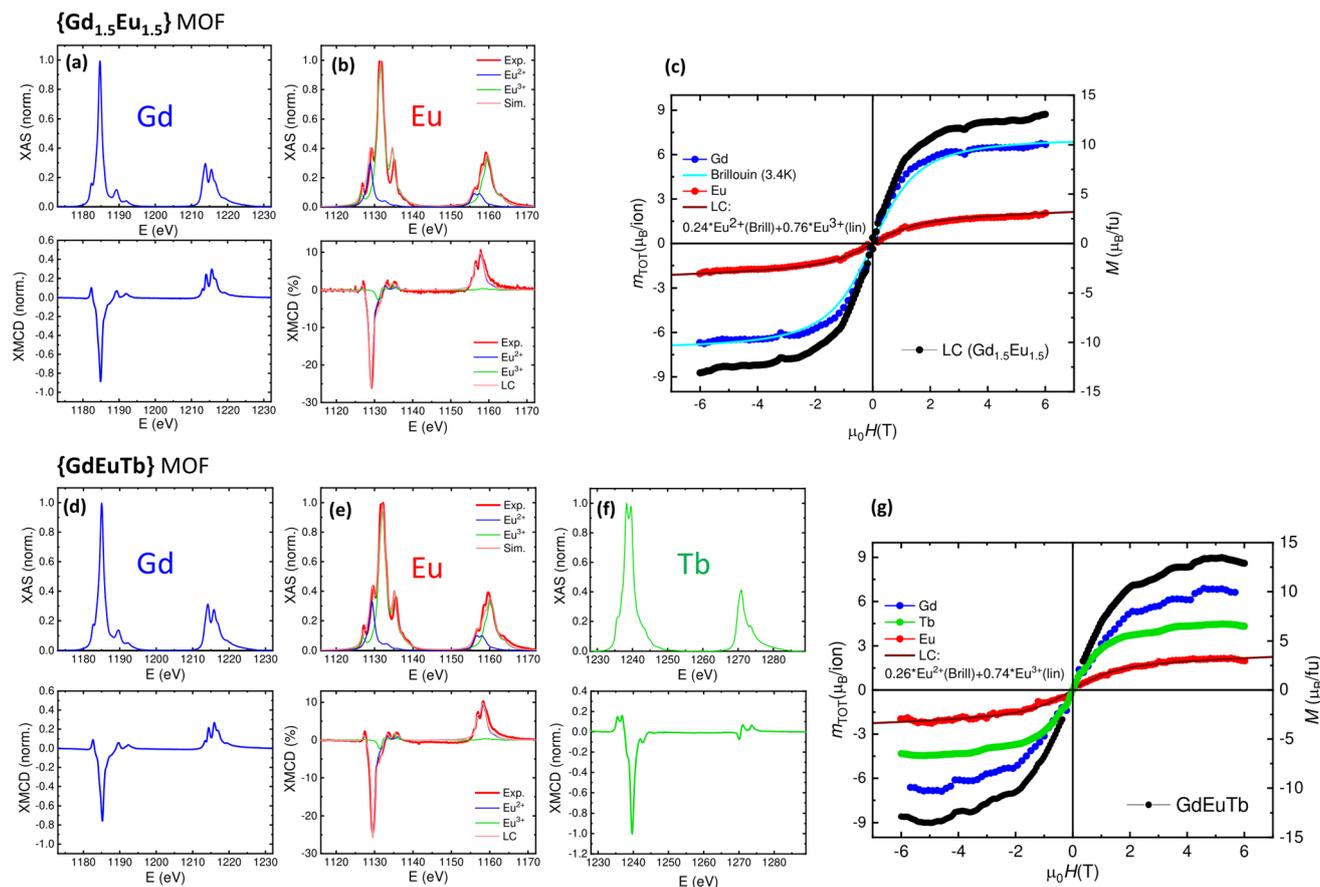*J. Mater. Chem. A*, 2024, **12**, 21971–21986 | **21977**

Fig. 4 XAS and XMCD characterization. **$Gd_{1.5}Eu_{1.5}$**: normalized, background-subtracted XAS (top) and XMCD (bottom) spectra measured at 6 T at 3.4 K across the $M_{4,5}$ edge of Gd (a) and (b) Eu (also shown, the simulated spectra for Eu^{2+} and Eu^{3+}); (c) field-dependence of the total magnetic moment, $m_{TOT}(H)$/ion, obtained for Gd^{3+} and Eu, and calculated magnetic moment per formula unit, at 3.4 K. **GdEuTb**: XAS and XMCD (6 T at 3.4 K) across the $M_{4,5}$ edges of Gd (d), (e) Eu (also shown, simulated spectra for Eu^{2+} and Eu^{3+}), and (f) Tb; (g) $m_{TOT}(H)$/ion obtained for Gd^{3+}, Eu and Tb^{3+}, and calculated magnetic moment per formula unit, at 3.4 K.

In the case of **$Gd_{1.5}Eu_{1.5}$**, the XAS and XMCD spectra of Europium reveal the coexistence of two valence states, Eu^{3+} and Eu^{2+}. Notably, the experimental spectra could be successfully reproduced considering the linear combination (LC) of the XAS-XMCD spectra calculated using Ligand Field Multiplet (LFM) simulations, implemented in Quanty–Crispy, for both Eu^{2+} and Eu^{3+}, in a ratio of 24–76% (refer to Fig. 4b). The presence of both Eu^{2+} and Eu^{3+} ions had been already inferred from magnetometric measurements of the mixed MOF (as discussed above, see Fig. 2g and h), and is here confirmed through the application of the XAS-XMCD element-selective technique. However, it is noted that the Eu^{2+}/Eu^{3+} ratio determined by the synchrotron measurements is higher than that obtained through SQUID ($Eu^{2+}/Eu^{3+} = 0.05/0.95$). The reason for this discrepancy may be attributed to the propensity of Eu in these carborane-based MOF to undergo photoreduction upon soft X-ray irradiation, not causing molecular damage.[115] For Europium, the XMCD signal arises from the magnetic Eu^{2+} ions, while the XAS absorption spectrum is associated to all Eu ions. Thus, we calculated the "averaged" magnetic moment per Eu ion in the sample, applying the sum rules with an averaged number holes $n_h = 7.8$, taking into account the experimentally determined

ratio $Eu^{2+}(Eu^{3+}) = 0.24(0.76)$, and the number of holes of each one, $n_h = 7$ (Eu^{2+}), 8 (Eu^{3+}). The $m_{TOT}(H)$/ion curves determined at 3.4 K both for Gd and Eu ions, together with the magnetic moment calculated per **$Gd_{1.5}Eu_{1.5}$** formula unit are shown in Fig. 4c. The $m_{TOT}(H)$/ion curve obtained for Gd^{3+} is in agreement with the Brillouin prediction at 3.4 K, while the $m_{TOT}(H)$/ion per average Eu coincides with theoretical curve, calculated as the LC of 24% of Eu^{2+} ions (following a Brillouin function) and 76% of Eu^{3+}.

In trinuclear **GdEuTb** MOF the XAS and XMCD spectra of Europium again show the coexistence of Eu^{3+} and Eu^{2+}, in a ratio of $Eu^{2+}/Eu^{3+} = 0.26/0.74$, estimated from LFM simulations (Fig. 4e), very similar to that found in the above discussed **$Gd_{1.5}Eu_{1.5}$** instance. The XAS-XMCD spectra across the $M_{4,5}$ edge of Terbium (Fig. 4f) corresponds to Tb(III) and are similar to the spectra described for Tb dinuclear **$Gd_{1.5}Tb_{1.5}$**. The $m_{TOT}(H)$/ion curves at 3.4 K obtained for Gd, Eu and Tb ions, along the magnetic moment calculated per **GdEuTb** formula unit are plotted in Fig. 4g. Once again, the $m_{TOT}(H)$/ion curve obtained for Gd^{3+} aligns with the Brillouin prediction at 3.4 K, the $m_{TOT}(H)$/ion for Tb^{3+} is similar to the curve measured for Tb-MOF and Tb in dinuclear **$Gd_{1.5}Tb_{1.5}$**, and the $m_{TOT}(H)$/ion per

21978 | *J. Mater. Chem. A*, 2024, **12**, 21971–21986

This journal is © The Royal Society of Chemistry 2024

Eu coincides with the theoretical curve, calculated as a weighted combination of Eu^{2+} and Eu^{3+} contribution, with the experimentally determined ratio.

MCE at atomic and macroscopic level

XMCD measurements were further used to characterize the MCE performance at atomic level, and compare it with the global MCE observed for the mixed MOF. The procedure is illustrated in Fig. 5, for the case of **Gd₁.₅Dy₁.₅**. XMCD(H) cycles at different fixed temperatures between 3.4 K and 18 K were measured separately for Gd^{3+} and Dy^{3+}. XAS-XMCD spectra at 6 T and each fixed temperature were performed (see Fig. 3a and b), to scale the XMCD(H) curves and obtain $m_{TOT}(H)$/ion isotherms both for Gd^{3+} (Fig. 5a) and Dy^{3+} (Fig. 5c). These figures show also, for comparison, the $M(H, T)$ curves for Gd^{3+} ions, according to Brillouin predictions (Fig. 5a, lines), and $M(H)$ isotherms measured by SQUID for Dy-MOF (Fig. 5c, lines). Maxwell method was then used to obtain, separately, the magnetic entropy change curves, $-\Delta S_m(T)$ for different ΔB values, for Gd^{3+} (Fig. 5b) and Dy^{3+} (Fig. 5d). Despite the error committed in the determination of $-\Delta S_m(T)$ from XMCD, associated to some thermal drift at intermediate temperatures, and the differentiation steps involved in Mawell method, the obtained cationic $-\Delta S_m(T)$ are close to the expected curves for homonuclear Gd-MOF and Dy-MOFs (also represented as continuous lines in Fig. 5b and d, for comparison purposes).

The total magnetic moment per **Gd₁.₅Dy₁.₅** formula unit, obtained from the LC of $m_{TOT}(H)$/ion contributions at different temperatures is shown in Fig. 5e (bold symbols), along the $M(H, T)$ curves obtained by magnetometry (open symbols). A good agreement is observed for those curves measured in similar T conditions.

Finally, the macroscopic magnetic entropy change $-\Delta S_m(T, H)$ per formula unit, calculated as the LC of the individual cationic contributions obtained for Gd and Dy, is shown in Fig. 5f (bold symbols). The obtained curves are in reasonably agreement with the $-\Delta S_m(T, H)$ directly determined from the $M(T, H)$ curves of **Gd₁.₅Dy₁.₅** MOF (shown in Fig. 5f as open symbols), within the associated errors of the procedure. These results showcase two aspects. On the one hand, they underscore the potential of XMCD technique for investigating the individual MCE performance of distinct ions within magnetically complex materials. On the other, they reveal that in these mixed {GdLn} MOFs, the MCE is the sum of the separate ions' contributions, indicating an additive behavior.

Dynamic magnetic properties

To characterize the spin magnetic relaxation properties of the synthesized {GdLn} MOFs, we performed ac susceptibility measurements as a function of the frequency, temperature and magnetic field. Fig. 6 (left) shows the out-of-phase component of the susceptibility as a function of the frequency, at constant
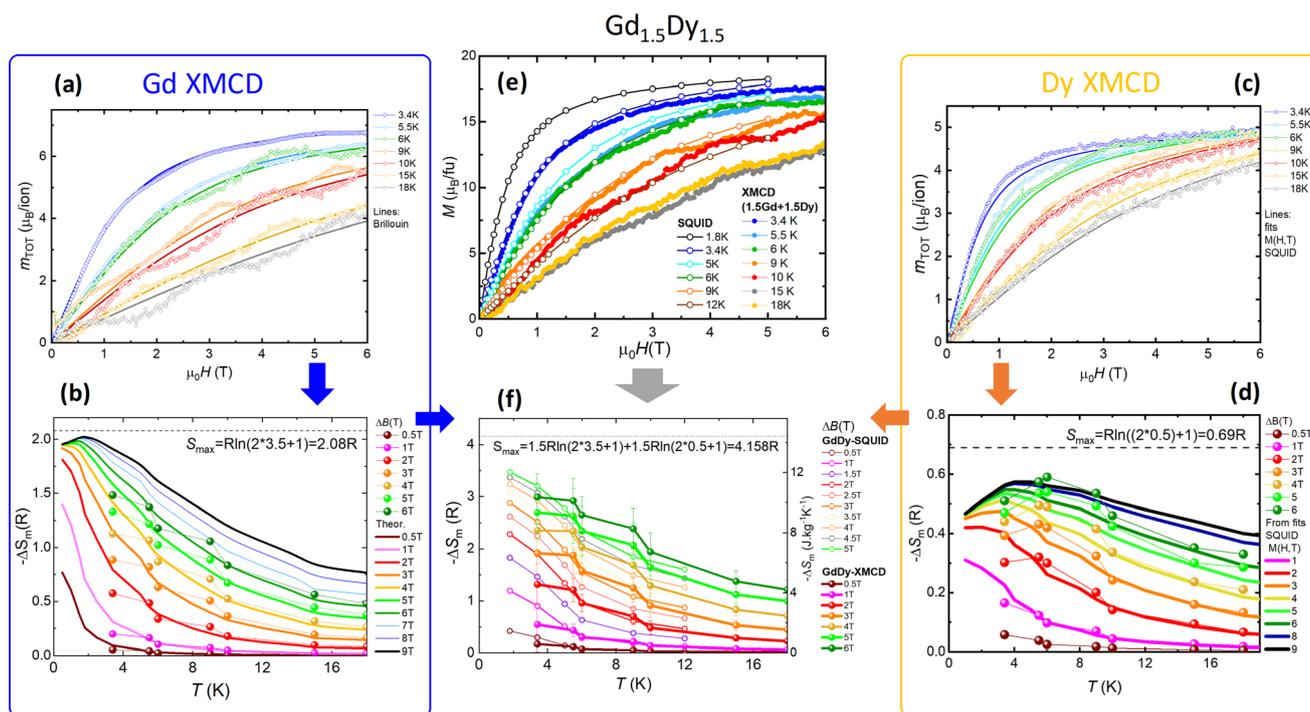

Fig. 5 MCE at atomic and macroscopic level. Lateral panels: $m_{TOT}(H)$/ion curves determined by XMCD at different temperatures for Gd^{3+} (a) and Dy^{3+} (c), and derived magnetic entropy change curves, $-\Delta S_m(T, H)$, for Gd^{3+} (b) and Dy^{3+} (d). Central panel: (e) magnetization per formula unit as a function of field at different temperatures, $M(H, T)$, obtained as the linear combination of XMCD-obtained $m_{TOT}(H)$/ion curves (bold symbols) and measured by SQUID (open symbols); (f) total magnetic entropy change $-\Delta S_m(T, H)$ per formula unit, calculated as the linear combination of the individual cationic contributions (bold symbols). For comparison, the $-\Delta S_m(T, H)$ obtained from the $M(T, H)$ curves of **Gd₁.₅Dy₁.₅** MOF are shown (open symbols). In (b), (d) and (f) the dotted lines indicate the maximum available entropy.
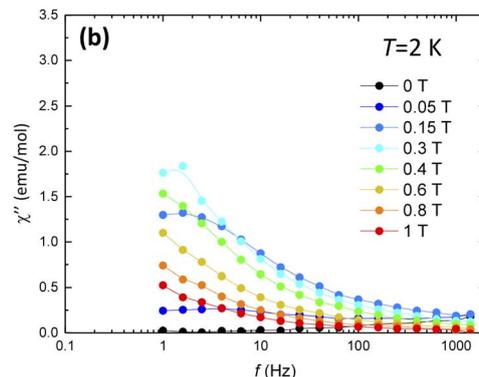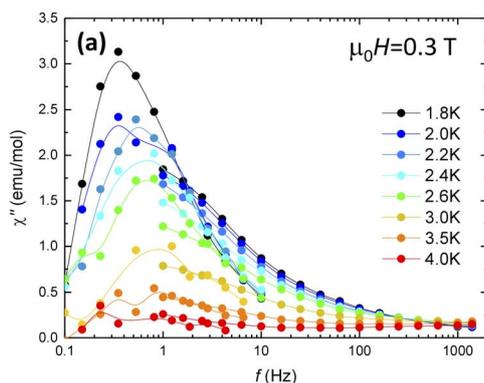
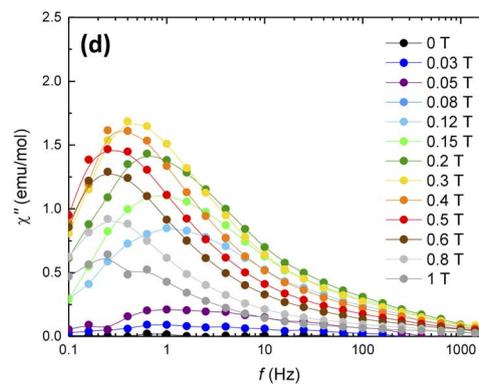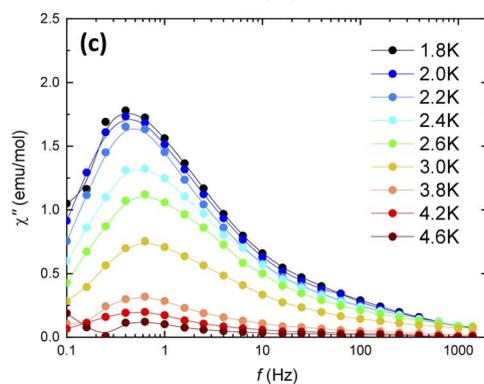This journal is © The Royal Society of Chemistry 2024

J. Mater. Chem. A, 2024, **12**, 21971–21986 | **21979**
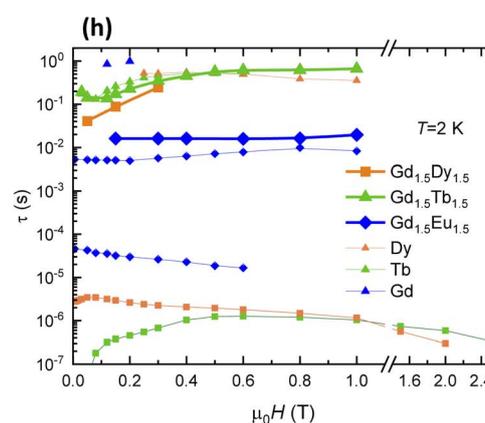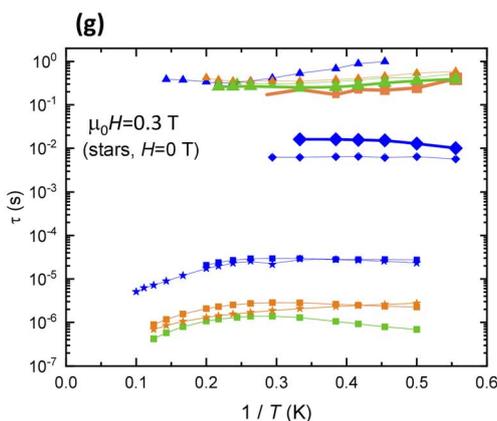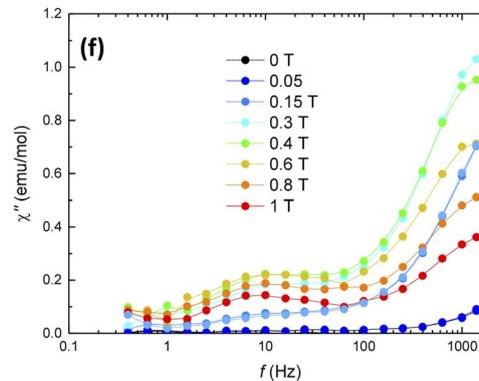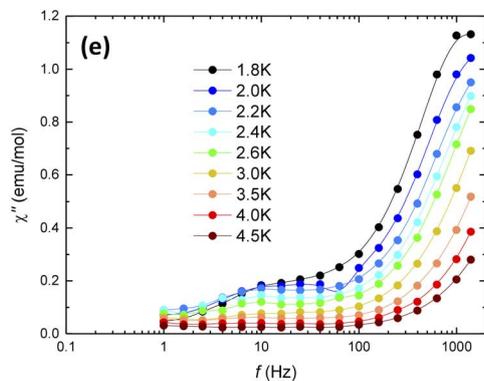
Fig. 6 Spin magnetic relaxation of mixed {GdLn} MOFs. (Left: a, c, e and g): imaginary component of the ac susceptibility as a function of the frequency, $\chi''(f)$, at $\mu_0H = 0.3$ T, and (right: b, d, f and h): at $T = 2$ K and different applied magnetic fields. (Bottom): (g) magnetic relaxation time as a function of the inverse temperature ($1/T$) at $\mu_0H = 0.3$ T and (h) as a function of the applied magnetic field at $T = 2$ K, for the different relaxation processes observed. For comparison, relaxation times previously reported for homonuclear Gd, Tb and Dy-MOFs are shown (open symbols).[114,115] Additional relaxation results for {GdTbEu} MOF are shown in Fig. S4.†

21980 | *J. Mater. Chem. A*, 2024, **12**, 21971–21986

This journal is © The Royal Society of Chemistry 2024

$\mu_0 H = 0.3$ T and different temperatures between 1.8 K–20 K, $\chi''(f, T)$, while Fig. 6 (right) plots the $\chi''(f, H)$ curves, at fixed $T = 1.8$ K and different applied magnetic fields in the 0–1 T range. From these data, the spin relaxation time for the different relaxation processes observed were obtained. Fig. 6g and h show, respectively, the dependence of the relaxation time with the inverse of the temperature, $\tau(1/T)$, and the magnetic field, $\tau(H)$, obtained for the different process in all studied {GdLn} MOFs. Results are discussed in the light of measurements previously reported for homonuclear Gd, Tb and Dy MOFs.[114,115]

For **Gd$_{1.5}$Dy$_{1.5}$** MOF, under the application of a $\mu_0 H = 3$ T magnetic field, a slow relaxation process at $f < 1$ Hz, and a second process is hinted at the highest measured $f = 1$ kHz (Fig. 6a and b). Both the $\chi''(f, T, 0.3 \text{ T})$ and $\chi''(f, H, 2 \text{ K})$ resemble the curves measured for the homonuclear analogue Dy-MOF, though the curves in the mixed MOF are slightly shifted toward lower frequencies. The relaxation peaks associated to Gd are not observed, possibly masked by the much larger intensity of the Dy ones.

Similarly, in the case of **Gd$_{1.5}$Tb$_{1.5}$** MOF the $\chi''(f, T, 0.3 \text{ T})$ and $\chi''(f, H, 2 \text{ K})$ curves display a single very low frequency peak (Fig. 6b and c), with $\tau(1/T)$, and $\tau(H)$ dependencies similar to those previously observed for homonuclear Tb-MOF, which can be associated to a direct process. Like in the previous case, the

relaxation is dominated by the anisotropic ion, and the processes associated to Gd are not observed.

In contrast, in **Gd$_{1.5}$Eu$_{1.5}$** MOF, the $\chi''(f, T, H)$ behavior (Fig. 6d and e) is very similar to that previously observed for Gd-MOF,[115] and evidences the single-ion relaxation of the Gd ions in the mixed MOF through multiple processes. The first relaxation slow process has relaxation time values in the order of $\tau_1 \approx 0.1$ to 1 s. The $\tau_1(1/T)$ dependence at 0.3 T could be fit to an Arrhenius law with an activation energy of $U/k_B = 12.1$ K, of the same order as the levels splitting. The second slowest relaxation process, with a T and H independent relaxation time constant $\tau_2 \approx 0.016$ s may be associated to a direct process. The third, temperature-dependent relaxation process (τ_3) may be ascribed to a Resonant Phonon Trapping (RPT) mechanism.[118–120]

Finally, the dynamic behavior of trinuclear **GdTbEu** MOF (Fig. S4†) is very similar to that of previously discussed **Gd$_{1.5}$Tb$_{1.5}$**, *i.e.* it is dominated by the intensity of Tb relaxation.

Optical properties

The absorption spectra of the new {GdLn} MOFs exhibit a slight broadening of the UV band, akin to that observed for the free ligand *m*CB-L and reminiscent of the UV absorption bands in previous mono- and multi-metallic MOFs (Fig. S3†). The
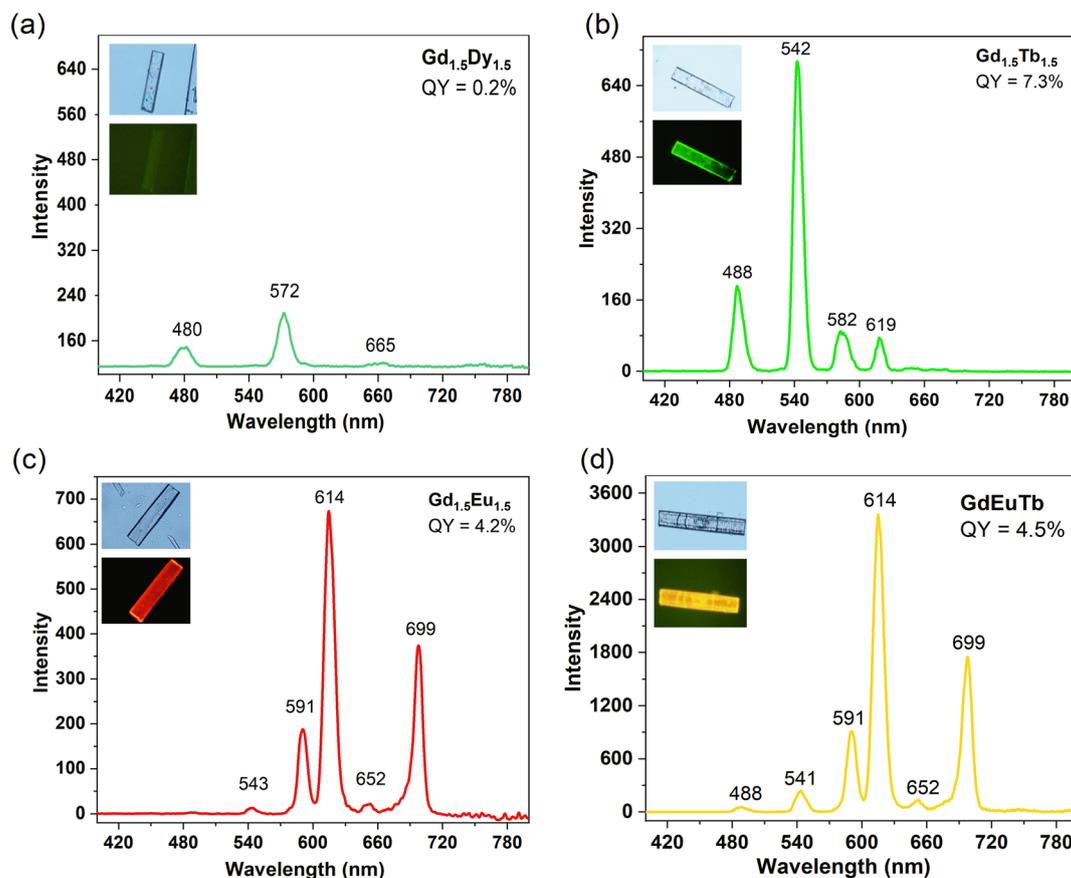
Fig. 7 Luminescent properties of mixed {GdLn} MOFs. Solid-state emission spectra of **Gd$_{1.5}$Dy$_{1.5}$** (a), **Gd$_{1.5}$Tb$_{1.5}$** (b), **Gd$_{1.5}$Eu$_{1.5}$**(c) and **GdEuTb** (d) under continuous-wave irradiation ($\lambda_{exc} = 280$ nm) at room temperature. (Insets): Quantum yields (QY) and optical microscopy images of the corresponding crystals under white and the corresponding luminescence images.

This journal is © The Royal Society of Chemistry 2024

J. Mater. Chem. A, 2024, **12**, 21971–21986 | **21981**

emission spectra in the visible region for powdered samples of all the studied mixed {GdLn} MOFs under light irradiation (λ_{ex} = 280 nm; air atmosphere; RT) are shown in Fig. 7 and Table S2.† No blue emission originating from the ligand is detected. The spectra of **Gd₁.₅Dy₁.₅**, **Gd₁.₅Tb₁.₅** and **Gd₁.₅Eu₁.₅** show solely the characteristic emission peaks for, respectively, Dy^{3+} (λ_{max}^{em} = 572 nm), Tb^{3+} (λ_{max}^{em} = 542 nm, deriving from $^5D_4 \rightarrow {}^7F_J$ (J = 6–3)) and Eu^{3+} (λ_{max}^{em} = 614 nm, $^5D_0 \rightarrow {}^7F_j$; J = 1–4),[20] while the spectrum of trinuclear **GdEuTb** includes the peaks of both Eu^{3+} and Tb^{3+}, with resulting emission color ranging from green (**Gd₁.₅Tb₁.₅**), red (**Gd₁.₅Eu₁.₅**), to greenish (**Gd₁.₅Dy₁.₅**) and yellow (**GdEuTb**), see Fig. 7 (insets) and S5.† In the case of the tri-metallic **GdEuTb** MOF, the emitted color is due to the combination of the two extreme colors (green and red) for the individual Tb^{3+} and Eu^{3+} lanthanides, respectively (Fig. 7).[15] No emission is observed from Gd. This fact is justified by the fact that the calculated triplet state (T_1) energy of mCB-L is not enough to sensitize the Gd. The measured quantum yield (QY) values (Table S2†) of all MOFs are 0.2% (**Gd₁.₅Dy₁.₅**), 7.3% (**Gd₁.₅Tb₁.₅**), 4.2% (**Gd₁.₅Eu₁.₅**) and 4.5% (**GdEuTb**). The emission of the Tb/Eu-containing MOFs (**Gd₁.₅Tb₁.₅**, **Gd₁.₅Eu₁.₅**, **GdEuTb**), are dominated by Tb^{3+} and Eu,[3] but have significantly lower QY than the values previously reported for carborane-based pure Tb (49.8%), Eu (20.5%) and mixed $Tb_{0.5}Eu_{0.5}$ (42.5%) MOFs.[20] We speculate that the energy of the excited carboranes next to the Gd ions is lost through non-radiative pathways, not contributing to the sensitization of the Tb, Eu or Dy atoms, reducing the overall MOF quantum yield. Mono-exponential fitting of the slower part of the decay curves was carried out to obtain the longest luminescence lifetimes, while avoiding possible background interferences (Fig. S6†). The obtained lifetimes for the **Gd₁.₅Dy₁.₅** (37.3 μs), **Gd₁.₅Tb₁.₅** (872.5 μs), **Gd₁.₅Eu₁.₅** (739.1 μs) and **GdEuTb** (744.1 for Eu^{3+}, 867.1 for Tb^{3+}) are nearly identical to those of the individual Dy-MOF (41.7 μs), Tb-MOF (849.7 μs) and Eu-MOF (739.0 μs),[20] suggesting no energy transfer (ET) occurs between Ln ions. Since no rise is observed in the first part of the decay signal, we conclude that no sensitization from one lanthanide to the other is occurring, nor even from the non-emitting Gd, as consequence of the fact that it was not sensitized by the carborane. Furthermore, contrarily to that observed in previous carborane-based binary Eu/Tb MOFs, in the trinuclear **GdEuTb**, there is no ET between Eu and Tb ions, indicating that the inclusion of Gd separating the ions hinders the energy transfer.

Discussion

Finally, we discuss the multifunctional properties of the new carborane-based mixed {GdLn} MOFs, in view of the above described magneto-thermal and optical characterization results. All {GdLn} compounds exhibit MCE, with entropy change values $-\Delta S_m$ at 1.8 K and ΔB = 2–0 T, in decreasing order, of 7.90, 7.28, 4.94 and 4.84 J kg⁻¹ K⁻¹ for **Gd₁.₅Dy₁.₅**, **Gd₁.₅Tb₁.₅**, **GdEuTb** and **Gd₁.₅Eu₁.₅**. Although, as expected, these values are smaller than those of homonuclear Gd MOF, the mixed MOFs have interesting added functionalities. Both **Gd₁.₅Tb₁.₅** and **Gd₁.₅Dy₁.₅** MOFs exhibit field-induced slow

relaxation of the magnetization arising from the anisotropic Ln = Dy and Tb SMM units, associated to a direct process. Since the relaxation time associated to this mechanism is essentially field-independent above 2 T, the MCE may be used to refrigerate the SMM units. However, it should be noted that for the cooling procedure, a change of magnetic field $\Delta B = B_f - B_i$ with $B_i \neq 0$ should be used, since no relaxation is observed in the absence of field (Fig. 6h). In addition, **Gd₁.₅Tb₁.₅** displays green luminescent emission, while **Gd₁.₅Dy₁.₅** MOF's emission is greenish but its quantum yield is quenched. On the other hand, **Gd₁.₅Eu₁.₅** exhibits slow magnetic relaxation arising from Gd, with a relaxation time $\tau \sim 0.02$ s that could be maintained upon a refrigeration cycling under $\Delta B = B_f - B_i$ with $B_i > 2$ T, and displays red luminescence. Finally, **GdEuTb** MOF exhibits MCE along yellow luminescent emission.

Conclusions

The synthesis and full structural, magneto-thermal and optical properties of new carborane-based mixed MOFs {[(GdLn)₃(mCB-L)₄(NO₃)(DMF)$_x$]$_n$·Solv} incorporating Ln = Dy, Tb, or Tb/Eu have been reported. The use of the mCB-L ligand allows the synthesis of isostructural multivariate MOFs combining any tailored combination of lanthanides with desired ratios, and therefore is ideal for the preparation of multifunctional materials. Herein we explored the potentiality of combining Gd, providing the largest change of entropy for magnetocalorics, with different lanthanides introducing added functionalities. We demonstrate that **Gd₁.₅Ln₁.₅** (Ln = Tb, Dy) constitute multifunctional MOFs incorporating MCE, field-induced slow relaxation of the magnetization, and green emission, in the case of Ln = Tb. Conversely, **Gd₁.₅Ln₁.₅** (Ln = Eu, Eu/Tb) exhibit MCE, field-induced slow relaxation of the magnetization for Ln = Gd, and red/yellow luminescent emission for Ln = Eu and Eu/Tb substitutions, respectively. Interestingly, the coexistence of MCE and SMM properties would permit "self-refrigeration" of the magnetic units, using an applied magnetic field change with non-zero smallest field. Although in these MOFs magnetic bifunctionality was not observed, the concept of self-refrigerated nanomagnets in mixed MOFs is worth pursuing.

Previous studies of mixed Gd/Ln MOFs had focused either on the luminescent or magnetocaloric properties of the compounds. Our comprehensive study of the optical, thermal, dc and ac magnetic properties has allowed us to establish how the macroscopic properties of the {GdLn} MOFs benefit from those of the constituting elements. Macroscopic magnetometry measurements allowed characterizing the magnetic and MCE behaviour of the mixed MOFs, while element-selective XAS-XMCD was crucial for analyzing the magnetic properties of the individual Ln ions. The use of this rarely employed technique for MOF characterization allowed us to show how global MCE properties emerge from the contributions of constituent lanthanides. This novel methodology holds promise to advance research of other multimetallic magnetocaloric materials, including high-entropy (HE) alloys, with significant potential for energy-efficient refrigeration.

21982 | *J. Mater. Chem. A*, 2024, **12**, 21971–21986

This journal is © The Royal Society of Chemistry 2024

We have shown that in these carborane-based mixed MOFs the static magnetic and MCE properties results from the additive contribution of the constituent Ln elements. The dynamic properties of $Gd_{1.5}Ln_{1.5}$ (Ln = Dy, Tb, Tb/Eu) are dominated by the anisotropic Ln = Tb, Dy, while those of $Gd_{1.5}Eu_{1.5}$ reflect the relaxation of the magnetic Gd ion. On the other hand, color tuning ranging from green ($Gd_{1.5}Tb_{1.5}$), red ($Gd_{1.5}Eu_{1.5}$), to greenish ($Gd_{1.5}Dy_{1.5}$) and yellow ($GdEuTb$) was achieved through the combination of lanthanide ions, although quantum yield efficiency was diminished with respect to that of homonuclear MOFs due to the presence of Gd ion.

In conclusion, our innovative synthetic approach for preparing multi-lanthanide MOFs not only expands the horizons for investigating "complex magnetic materials", but also paves the way for developing multifunctional MOFs endowed with tailored or unforeseen properties. Specifically, {GdLn} MOFs offer the attractive possibility of organizing self-refrigerated SMM memory units and "qubits", for high density information storage and quantum computing applications, requiring operation at cryogenic temperatures.

At present, Artificial Intelligence (AI) algorithms are already being exploited in the realm of high-entropy alloys, comprising five or more metals, to predict materials with novel synergistic properties.[121,122] Looking ahead, we anticipate the application of AI in uncovering new multi-lanthanide MOFs that exhibit compelling characteristics. However, this Machine Learning approach is contingent on the prior synthesis and thorough characterization of a substantial number of MOFs encompassing various combinations of lanthanides. Our work stands as a milestone in this promising direction, laying the foundation for future advancements in the discovery of innovative multi-lanthanide MOFs with remarkable properties.

Data availability

Data supporting this article have been included as part of the ESI.†

Author contributions

ZL, JGP synthesis, XRD, SEM-EDX, luminescent investigation and data curation; CR luminescence resources and writing; AA magnetometry resources, EB investigation and data curation; EB MCE and XAS-XMCD investigation and data curation; EB writing – original draft; JGP writing – review; EB conceptualization; EB and JGP supervision, resources, project administration. All authors have given approval to the final version of the manuscript.

Conflicts of interest

There are no conflicts to declare.

Acknowledgements

References

1 X. J. Wang, X. Zhang, R. Pandharkar, J. F. Lyu, D. Ray, Y. Yang, S. Kato, J. Liu, M. C. Wasson, T. Islamoglu, Z. Li, J. T. Hupp, C. J. Cramer, L. Gagliardi and O. K. Farha, *ACS Catal.*, 2020, **10**, 8995–9005.

2 D. Q. Yuan, D. Zhao, D. F. Sun and H. C. Zhou, *Angew. Chem.*, 2010, **49**, 5357–5361.

3 X. Zhang, V. Vieru, X. Feng, J.-L. Liu, Z. Zhang, B. Na, W. Shi, B.-W. Wang, A. K. Powell, L. F. Chibotaru, S. Gao, P. Cheng and J. R. Long, *Angew. Chem.*, 2015, **54**, 9861–9865.

4 K. Liu, X. Zhang, X. Meng, W. Shi, P. Cheng and A. K. Powell, *Chem. Soc. Rev.*, 2016, **45**, 2423–2439.

5 G. Mínguez Espallargas and E. Coronado, *Chem. Soc. Rev.*, 2018, **47**, 533–557.

6 R. E. Sikma, K. S. Butler, D. J. Vogel, J. A. Harvey and D. F. Sava Gallis, *J. Am. Chem. Soc.*, 2024, **146**, 5715–5734.

7 W. Jiang, C.-C. Liang and Y.-B. Zhang, *Adv. Funct. Mater.*, 2024, 2308946.

8 M. Viciano-Chumillas, X. Liu, A. Leyva-Pérez, D. Armentano, J. Ferrando-Soria and E. Pardo, *Coord. Chem. Rev.*, 2022, **451**, 214273.

9 C. Castillo-Blas, V. A. De la Peña-O'Shea, I. Puente-Orench, J. Romero de la Paz, R. Sáez-Puche, R. Gutierrez-Puebla and F. Gándara, *Sci. Adv.*, 2017, **3**, e1700773.

10 K. L. S. Abednatanzi, P. G. Derakhshandeh, H. Depauw, F.-X. Coudert, H. Vrielinck and P. Van Der Voort, *Chem. Soc. Rev.*, 2019, **48**, 2535–2565.

11 Y. Wang, Y.-Y. Xue, L.-T. Yan, H.-P. Li, Y.-P. Li, E.-H. Yuan, M. Li, S.-N. Li and Q.-G. Zhai, *ACS Appl. Mater. Interfaces*, 2020, **12**, 24786.

12 L. J. Wang, H. Deng, H. Furukawa, F. Gándara, K. E. Cordova, D. Peri and O. M. Yaghi, *Inorg. Chem.*, 2014, **53**, 5881.

13 X. Zhao, Z. Xue, W. Chen, X. Bai, R. Shi and T. Mu, *J. Mater. Chem. A*, 2019, **7**, 26238.

14 R. L. Vasile, A. A. Godoy, I. Puente Orench, N. M. Nemes, V. A. de la Peña O'Shea, E. Gutiérrez-Puebla, J. L. Martínez, M. Á. Monge and F. Gándara, *Chem. Mater.*, 2022, **34**, 7029–7041.

15 Z. Li, X.-B. Li, M. E. Light, A. E. Carrillo, A. Arauzo, M. Valvidares, C. Roscini, F. Teixidor, C. Viñas, F. Gándara, E. Bartolomé and J. G. Planas, *Adv. Funct. Mater.*, 2023, **33**, 2307369.

This journal is © The Royal Society of Chemistry 2024

J. Mater. Chem. A, 2024, **12**, 21971–21986 | **21983**

16 R. L. Vasile, R. S. J. Silva, E. Céspedes, J. L. Martínez, E. Gutiérrez-Puebla, M. A. Monge and F. Gándara, *Inorg. Chem.*, 2023, **62**, 19741–19748.

17 E. Bartolomé, A. Arauzo, S. Fuertes, L. Navarro-Spreafica, P. Sevilla, H. F. Cortés, N. Settineri, S. J. Teat and E. C. Sañudo, *Dalton Trans.*, 2023, **52**, 7258–7270.

18 Y. Cui, B. Chen and G. Qian, *Coord. Chem. Rev.*, 2014, **273–274**, 76–86.

19 Z. Qu, D. Wu, J. Jin, G. Yang and Y.-Y. Wang, *J. Solid State Chem.*, 2022, **309**, 123003.

20 Z. Li, R. Núñez, M. E. Light, E. Ruiz, F. Teixidor, C. Viñas, D. Ruiz-Molina, C. Roscini and J. G. Planas, *Chem. Mater.*, 2022, **34**, 4795–4808.

21 Y. Guo, Z. Han, H. Min, Z. Chen, T. Sun, L. Wang, W. Shi and P. Cheng, *Inorg. Chem.*, 2021, **60**, 9192–9198.

22 J.-M. Li, R. Huo, X. Li and H.-L. Sun, *Inorg. Chem.*, 2019, **58**, 9855–9865.

23 Q. Lin, W. Xie, Z. Zong, Z. Liu, Y. Sun and L. Liang, *New J. Chem.*, 2021, **45**, 7382–7389.

24 S. Mohapatra, B. Rajeswaran, A. Chakraborty, A. Sundaresan and T. K. Maji, *Chem. Mater.*, 2013, **25**(25), 1673–1679.

25 D. B. Kanzariya, M. Y. Chaudharya and T. K. Pal, *Dalton Trans.*, 2023, **52**, 7383–7404.

26 G. Lorusso, J. W. Sharples, E. Palacios, O. Roubeau, E. K. Brechin, R. Sessoli, A. Rossin, F. Tuna, E. J. L. McInnes, D. Collison and M. Evangelisti, *Adv. Mater.*, 2013, **25**, 4653–4656.

27 G. Lorusso, E. Natividad, M. Evangelisti and O. Roubeau, *Mater. Horiz.*, 2019, **6**, 144–156.

28 M. Falsaperna and P. Saines, *Dalton Trans.*, 2022, **51**, 3394–3410.

29 P. Konieczny, W. Sas, D. Czernia, A. Pacanowska, M. Fitta and R. Pełka, *Dalton Trans.*, 2022, **51**, 12762–12780.

30 C.-L. Chen, C. Wang, X.-Y. Zheng, R. Zhang, Y. Xu, G.-L. Zhuang, L.-S. Long, L.-S. Zheng, X.-J. Kong and Y. Cao, *J. Am. Chem. Soc.*, 2023, **145**, 16983–16987.

31 E. Coronado, *Nat. Rev. Mater.*, 2020, **5**, 87–104.

32 M. J. Graham, J. M. Zadrozny, M. S. Fataftah and D. E. Freedman, *Chem. Mater.*, 2017, **29**, 1885–1897.

33 N. Ishikawa, M. Sugita, T. Ishikawa, S. Y. Koshihara and Y. Kaizu, *J. Am. Chem. Soc.*, 2003, **125**, 8694–8695.

34 E. Bartolomé, A. Arauzo, J. Luzón, J. Bartolomé and F. Bartolomé, in *Handbook of Magnetic Materials*, ed. E. Brück, Elsevier, 2017, pp. 1–289.

35 L. Sorace and D. Gatteschi, *Electronic Structure and Magnetic Properties of Lanthanide Molecular Complexes*, ed. R. Layfield and M. Murugesu, Wiley-VCH, 2015.

36 Z. Zhu, C. Zhao, T. Feng, X. Liu, X. Ying, X.-L. Li, Y.-Q. Zhang and J. Tang, *J. Am. Chem. Soc.*, 2021, **143**, 10077–10082.

37 F. S. Guo, B. M. Day, Y. C. Chen, M. L. Tong, A. Mansikkamäki and R. A. Layfield, *Science*, 2018, **362**, 1400–1403.

38 A. Gaita-Ariño, F. Luis, S. Hill and E. Coronado, *Nat. Chem.*, 2019, **11**, 301–309.

39 M. D. Jenkins, Y. Duan, B. Diosdado, J. J. García-Ripoll, A. Gaita-Ariño, C. Giménez-Saiz, P. J. Alonso, E. Coronado and F. Luis, *Phys. Rev. B*, 2017, **95**, 064423.

40 F. Luis, P. J. Alonso, O. Roubeau, V. Velasco, D. Zueco, D. Aguilà, J. I. Martínez, L. A. Barrios and G. Aromí, *Commun. Chem.*, 2020, **3**, 176.

41 M. Urdampilleta, S. Klyatskaya, M. Ruben and W. Wernsdorfer, *Phys. Rev. B: Condens. Matter Mater. Phys.*, 2013, **87**, 195412.

42 C. Godfrin, A. Ferhat, R. Ballou, S. Klyatskaya, M. Ruben, W. Wernsdorfer and F. Balestro, *Phys. Rev. Lett.*, 2017, **119**, 187702.

43 C. Zhang, X. Ma, P. Cen, X. Jin, J. Yang, A. Y.-Q. Zhang, J. Ferrando-Soria, E. Pardo and X. Liu, *Dalton Trans.*, 2020, **49**, 14123–14132.

44 L. Li, Y. Fang, S. Liu, M. Hu and W. Wang, *J. Rare Earths*, 2023, **41**, 100–107.

45 C. Bai, C.-T. Li, H.-M. Hu, B. Liu, J.-D. Li and G. Xue, *Dalton Trans.*, 2019, **48**, 814–817.

46 Z. Chen, B. Zhao, P. Cheng, X. Q. Zhao, W. Shi and Y. Song, *Inorg. Chem.*, 2009, **48**, 3493–3495.

47 T. Yang, S. Wang, C. Lin, X. Wang, B. Zhu and D. Wu, *Dalton Trans.*, 2021, **50**, 1293–1299.

48 A. Calahorro, I. Oyarzabal, B. Fernandez, J. Seco, T. Tian and D. Fairen-Jimenez, *Dalton Trans.*, 2016, **45**, 591–598.

49 R. Gao, F. Guo, N. Bai, Y. Wu, F. Yang and J. Liang, *Inorg. Chem.*, 2016, **55**, 11323–11330.

50 J. López-Cabrelles, L. Escalera-Moreno, Z. Hu, H. Prima-García, G. Mínguez-Espallargas, A. Gaita-Ariño and E. Coronado, *Inorg. Chem.*, 2021, **60**, 8575–8580.

51 A. Urtizberea, E. Natividad, P. J. Alonso, M. A. Andrés, I. Gascón, M. Goldmann and O. Roubeau, *Adv. Funct. Mater.*, 2018, **28**, 1801695.

52 Y. Zhang, W. Hao, C. Hu, X. Wang, X. Zhang and L. Li, *Adv. Funct. Mater.*, 2023, **33**, 2310047.

53 C. Romero-Muñiz, J. Y. Law, J. Revuelta-Losada, L. Moreno-Ramírez and V. Franco, *Innovation Mater.*, 2023, **1**, 100045.

54 Y. Zhang, W. Hao, J. Shen, Z. Mo, T. Gottschall and L. Li, *Acta Mater.*, 2024, **276**, 120128.

55 P. W. Doheny, J. Chen, T. Gruner, F. M. Groscheb and P. J. Saines, *J. Mater. Chem. A*, 2023, **11**, 26474–26480.

56 Y. Zhang, Y. Tian, Z. Zhang, Y. Jia, B. Zhang, M. Jiang, J. Wang and Z. Ren, *Acta Mater.*, 2022, **226**, 117669.

57 Y. Zhang, J. Zhu, S. Li, Z. Zhang, J. Wang and Z. Ren, *Sci. China Mater.*, 2022, **65**, 1345.

58 J. Y. Law and V. Franco, in *Handbook on the Physics and Chemistry of Rare Earths*, 2023, vol. 64, pp. 175–246.

59 L. Li and M. Yan, *J. Mater. Sci. Technol.*, 2023, **136**, 1–12.

60 L. Li and M. Yan, *Alloys Compd.*, 2020, **823**, 153810.

61 R. J. C. Dixey and P. J. Saines, *Inorg. Chem.*, 2018, **57**, 12543–12551.

62 P. J. Saines, J. A. M. Paddison, P. M. M. Thygesen and M. G. Tucker, *Mater. Horiz.*, 2015, **2**, 528–535.

63 P. W. Doheny, S. J. Cassidy and P. J. Saines, *Inorg. Chem.*, 2022, **61**, 4957–4964.

64 S. Kim, R. Muhammad, K. Son and H. Oh, *Inorg. Chem.*, 2023, **62**, 2994–2999.

21984 | *J. Mater. Chem. A*, 2024, **12**, 21971–21986

This journal is © The Royal Society of Chemistry 2024

65 J. González, P. Sevilla, G. Gabarró-Riera, J. Jover, J. Echeverría, S. Fuertes, A. Arauzo, E. Bartolomé and E. C. Sañudo, *Angew. Chem.*, 2021, **60**, 12001–12006.

66 E. Bartolomé, A. Arauzo, S. Herce, A. Palau, N. Mestres, S. Fuertes, P. Sevilla, N. S. Settineri, L. Navarro-Spreafico, J. González and E. C. Sañudo, *Molecules*, 2021, **26**, 5503.

67 F.-G. Chen, W. Xu, J. Chen, H.-P. Xiao, H.-Y. Wang, Z. Chen and J.-Y. Ge, *Inorg. Chem.*, 2022, **61**, 5388–5396.

68 X.-Q. Ji, R. Sun, J. Xiong, H.-L. Sun and S. Gao, *J. Mater. Chem. C*, 2021, **9**, 15858–15867.

69 A. Arauzo, L. Gasque, S. Fuertes, C. Tenorio, S. Bernès and E. Bartolomé, *Dalton Trans.*, 2020, **49**, 13671–13684.

70 H. Brunckova, E. Mudra, L. Rocha, E. Nassar, W. Nascimento, H. Kolev, M. Lisnichuk, A. Kovalcikova, Z. Molcanova, M. Strečkova and L. Medvecky, *Inorganics*, 2021, **9**, 77.

71 X. Fan, S. Freslon, C. Daiguebonne, G. Calvez, L. Le Pollès, K. Bernot and O. Guillou, *J. Mater. Chem. C*, 2014, **2**, 5510–5525.

72 A. E. Psalti, D. Andriotou, S. A. Diamantis, A. Chatz-Giachia, A. Pournara, M. J. Manos, A. Hatzidimitriou and T. Lazarides, *Inorg. Chem.*, 2022, **61**, 11959–11972.

73 Y. Zheng, K. Liu, X. Sun, R. Guan, H. Su, H. You and C. Qi, *CrystEngComm*, 2015, **17**, 2321.

74 T. Alammar, I. Z. Hlova, S. Gupta, A. Biswas, T. Ma, L. Zhou, V. Balema, V. K. Pecharsky and A.-V. Mudring, *New J. Chem.*, 2020, **44**, 1054.

75 H. Brunckova, E. Mudra, L. Rocha, E. Nassar, W. Nascimento, H. Kolev, A. Kovalcikova, Z. Molcanova, M. Podobova and L. Medvecky, *Appl. Surf. Sci.*, 2021, **542**, 148731.

76 J. Rong, W. Zhang and J. Bai, *RSC Adv.*, 2016, **6**, 103714.

77 Y. Yang, L. Chen, F. Jiang, M. Yu, X. Wan, B. Zhangab and M. Hong, *J. Mater. Chem. C*, 2017, **5**, 1981.

78 K. Song, W. Xiao, M. He, J. Yu, Y. Bai and Y. Guan, *J. Photochem. Photobiol., A*, 2020, **389**, 112194.

79 T. Xia, W. Cao, L. Guan, J. Zhang, F. Jiang, L. Yua and Y. Wan, *Dalton Trans.*, 2022, **51**, 5426–5433.

80 A. Cadiau, C. D. S. Brites, P. M. F. J. Costa, R. A. S. Ferreira, J. Rocha and L. D. Carlos, *ACS Nano*, 2013, **7**, 7213–7218.

81 D. Zhao, X. Rao, J. Yu, Y. Cui, Y. Yang and G. Qian, *Inorg. Chem.*, 2015, **54**, 11193–11199.

82 T. Xia, J. Wang, K. Jiang, Y. Cui, Y. Yang and G. Qian, *Chin. Chem. Lett.*, 2018, **29**, 861–864.

83 Y. Zhao and D. Li, *J. Mater. Chem.*, 2020, **8**, 12739–12754.

84 B. P. Dash, R. Satapathy, J. A. Maguire and N. S. Hosmane, *New J. Chem.*, 2011, **35**, 1955–1972.

85 M. Scholz and E. Hey-Hawkins, *Chem. Rev.*, 2011, **111**, 7035–7062.

86 F. Issa, M. Kassiou and L. M. Rendina, *Chem. Rev.*, 2011, **111**, 5701–5722.

87 J. Plesek, *Chem. Rev.*, 1992, **92**, 269–278.

88 R. N. Grimes, *Carboranes*, Academic Press, 2016.

89 F. Teixidor and D. E. Kaufmann, *Science of Synthesis: Houben-Weyl Methods of Molecular Transformations*, Georg Thieme Verlag, Stuttgart, 5th edn, 2015, vol. 6.

90 S. Fujii, *MedChemComm*, 2016, **7**, 1082–1092.

91 J. F. Valliant, K. J. Guenther, A. S. King, P. Morel, P. Schaffer, O. O. Sogbein and K. A. Stephenson, *Coord. Chem. Rev.*, 2002, **232**, 173–230.

92 J. Poater, C. Viñas, I. Bennour, S. Escayola, M. Solà and F. Teixidor, *J. Am. Chem. Soc.*, 2020, **142**, 9396–9407.

93 J. Poater, M. Solà, C. Viñas and F. Teixidor, *Angew. Chem.*, 2014, **53**, 12191–12195.

94 J. Poater, C. Viñas, M. Solà and F. Teixidor, *Nat. Commun.*, 2022, **13**, 3844.

95 K. B. Idrees, K. O. Kirlikovali, C. Setter, H. Xie, H. Brand, B. Lal, F. Sha, C. S. Smoljan, X. Wang, T. Islamoglu, L. K. Macreadie and O. K. Farha, *J. Am. Chem. Soc.*, 2023, **145**, 23433–23441.

96 L. K. Macreadie, K. B. Idrees, C. S. Smoljan and O. K. Farha, *Angew. Chem., Int. Ed.*, 2023, **62**, e202304094.

97 O. K. Farha, A. M. Spokoyny, K. L. Mulfort, M. F. Hawthorne, C. A. Mirkin and J. T. Hupp, *J. Am. Chem. Soc.*, 2007, **129**, 12680–12681.

98 O. K. Farha, A. M. Spokoyny, K. L. Mulfort, S. Galli, J. T. Hupp and C. A. Mirkin, *Small*, 2009, **5**, 1727–1731.

99 S.-L. Huang, Y.-J. Lin, W.-B. Yu and G.-X. Jin, *Chempluschem*, 2012, **77**, 141–147.

100 Y.-S. Bae, A. M. Spokoyny, O. K. Farha, R. Q. Snurr, J. T. Hupp and C. A. Mirkin, *Chem. Commun.*, 2010, **46**, 3478–3480.

101 I. Boldog, P. J. Bereciartua, R. Bulánek, M. Kučeráková, M. Tomandlová, M. Dušek, J. Macháček, D. De Vos and T. Bāše, *CrystEngComm*, 2016, **18**, 2036–2040.

102 Y.-S. Bae, O. K. Farha, A. M. Spokoyny, C. A. Mirkin, J. T. Hupp and R. Q. Snurr, *Chem. Commun.*, 2008, 4135.

103 S.-L. Huang, L.-H. Weng and G.-X. Jin, *Dalton Trans.*, 2012, **41**, 11657–11662.

104 D. J. Clingerman, W. Morris, J. E. Mondloch, R. D. Kennedy, A. A. Sarjeant, C. Stern, J. T. Hupp, O. K. Farha and C. A. Mirkin, *Chem. Commun.*, 2015, **51**, 6521–6523.

105 D. J. Kennedy, R. D. Krungleviciute, V. Clingerman, J. E. Mondloch, Y. Peng, C. E. Wilmer, A. A. Sarjeant, R. Q. Snurr, J. T. Hupp, T. Yildirim, O. K. Farha and C. A. Mirkin, *Chem. Mater.*, 2013, **25**, 3539–3543.

106 L. Gan, E. Andres-Garcia, G. Mínguez Espallargas and J. G. Planas, *ACS Appl. Mater. Interfaces*, 2023, **15**, 5309–5316.

107 Z. Li, D. Choquesillo-Lazarte, J. Fraile, C. Viñas, F. Teixidor and J. G. Planas, *Dalton Trans.*, 2022, **51**, 1137–1143.

108 L. Gan, A. Chidambaram, P. G. Fonquernie, M. E. Light, D. Choquesillo-Lazarte, H. Huang, E. Solano, J. Fraile, C. Viñas, F. Teixidor, J. A. R. Navarro, K. C. Stylianou and J. G. Planas, *J. Am. Chem. Soc.*, 2020, **142**, 8299–8311.

109 S. Rodríguez-Hermida, M. Y. Tsang, C. Vignatti, K. C. Stylianou, V. Guillerm, J. Pérez-Carvajal, F. Teixidor, C. Viñas, D. Choquesillo-Lazarte, C. Verdugo-Escamilla, I. Peral, J. Juanhuix, A. Verdaguer, I. Imaz, D. Maspoch and J. Giner Planas, *Angew. Chem., Int. Ed.*, 2016, **55**, 16049–16053.

110 L. Gan, M. T. Nord, J. M. Lessard, N. Q. Tufts, A. Chidambaram, M. E. Light, H. Huang, E. Solano, J. Fraile, F. Suárez-García, C. Viñas, F. Teixidor,

This journal is © The Royal Society of Chemistry 2024

J. Mater. Chem. A, 2024, **12**, 21971–21986 | **21985**

K. C. Stylianou and J. G. Planas, *J. Am. Chem. Soc.*, 2023, **145**, 13730–13741.

111 M. A. Fox, *Icosahedral Carborane Derivatives*, Durham thesis, Durham University, 1991.

112 M. Shang, S. Liang, N. Qu, H. Lian and J. Lin, *Chem. Mater.*, 2017, **29**, 1813–1829.

113 F. Moro, V. Corradini, M. Evangelisti, R. Biagi, V. De Renzi, U. del Pennino, J. C. Cezar, R. Inglis, C. J. Milios and E. K. Brechin, *Nanoscale*, 2010, **2**, 2698–2703.

114 Z. Li, A. Arauzo, J. G. Planas and E. Bartolomé, *Dalton Trans.*, 2024, **53**, 8969–8979.

115 E. Bartolomé and J. Giner Planas, 2024, manuscript in preparation.

116 S. Tripathi, *XMCD investigation at M4,5 edges of the rare earth elements in high-performance permanent magnet*, PhD thesis, Max-Planck-Institut für Intelligente Systeme, Stuttgart, 2018.

117 B. Thole, P. Carra, F. Sette and G. van der Laan, *Phys. Rev. Lett.*, 1992, **68**, 1943–1946.

118 R. R. Schenker, M. N. Leuenberger, G. Chaboussant, D. Loss and H. U. Güdel, *Phys. Rev. B: Condens. Matter Mater. Phys.*, 2005, **72**, 184403–184413.

119 D. L. Huber, *Phys. Rev. B: Solid State*, 1965, **139**, A1684.15.08.2013.

120 A. Arauzo, A. Lazarescu, S. Shova, E. Bartolomé, R. Cases, J. Luzón, J. Bartolomé and C. Turta, *Dalton Trans.*, 2014, **43**, 12342–12356.

121 C. Wen, Y. Zhang, C. Wang, D. Xue, Y. Bai, S. Antonov, L. Dai and T. Lookman, *Acta Mater.*, 2019, **170**, 109–117.

122 G. Hart, T. Mueller, C. Toher and S. Curtarolo, *Nat. Rev. Mater.*, 2021, **6**, 730–755.

21986 | *J. Mater. Chem. A*, 2024, **12**, 21971–21986

This journal is © The Royal Society of Chemistry 2024